FAST AND CONTRAST-ENHANCED PHASE-SENSITIVE MAGNETIC RESONANCE IMAGING

A Dissertation

by

JONG BUM SON

Submitted to the Office of Graduate Studies of
Texas A&M University
in partial fulfillment of the requirements for the degree of

DOCTOR OF PHILOSOPHY

August 2007

Major Subject: Electrical Engineering

FAST AND CONTRAST-ENHANCED PHASE-SENSITIVE MAGNETIC RESONANCE IMAGING

A Dissertation

by

JONG BUM SON

Submitted to the Office of Graduate Studies of
Texas A&M University
in partial fulfillment of the requirements for the degree of

DOCTOR OF PHILOSOPHY

Approved by:

Chair of Committee,	Jim X. Ji
Committee Members,	Steven M. Wright
	Takis Zourntos
	Gerard L. Coté
Head of Department,	Costas N. Georghiades

August 2007

Major Subject: Electrical Engineering

ABSTRACT

Fast and Contrast-Enhanced Phase-Sensitive

Magnetic Resonance Imaging. (August 2007)

Jong Bum Son, B.S., Korea University

Chair of Advisory Committee: Dr. Jim Ji

Phase-sensitive magnetic resonance (MR) imaging has a number of important clinical applications, such as phase-sensitive inversion recovery (PSIR) and Dixon water/fat imaging. PSIR and Dixon techniques are widely used in neurological and body imaging to improve tissue-contrast, the former by extending the dynamic range of image intensity and the later by suppressing unnecessary fat signals. Several important limitations, however, occur in these techniques: (1) Dixon techniques cannot decompose two signals if the resonance frequencies are close. For example, in MR mammography, it is difficult to separate silicone breast implants signals (4.0 ppm) from fat signals (3.5 ppm); (2) the signal dynamic range of images acquired using Dixon techniques is limited by the equilibrium magnetization; and (3) long image acquisition time. These limitations have hindered the applications of phase-sensitive Dixon imaging techniques on breast implant imaging or as a screening tool where fast acquisition is required.

In this work, novel phase-sensitive MRI techniques were developed to

enhance the capability, image-contrast, and scan-efficiency of Dixon imaging techniques. Specifically, we developed (1) a generalized chemical-shift imaging technique to separate spectrally overlapped signals both T_1-contrast and chemical-shift; (2) a contrast-enhanced Dixon technique to extend the signal dynamic range of Dixon images; and (3) a single-echo acquisition (SEA) imaging technique integrated with phase-sensitive MR imaging to provide ultra-fast image acquisitions.

Phantom studies, performed on 1.5 T and 4.7 T MR scanners, demonstrated the developed generalized chemical-shift imaging technique could clearly separate breast silicone implant signals (4.0 ppm) from fat (3.5 ppm). The contrast-enhanced Dixon technique, by extending the dynamic range of signal intensity from positive levels to positive/negative levels, could improve image-contrast by 1.6 times, compared with a conventional single-point Dixon technique. Phantom studies, using a 64-channel SEA imaging system, showed the integrated Dixon technique with SEA could acquire decomposed 2-D water-only and fat-only images with ultra-fast frame-rates up to 1/TR, while providing improved image-contrast (by 2.4 times in this experiment) compared with a conventional SEA imaging technique.

ACKNOWLEDGMENTS

I would like to express appreciation to my committee chair, Dr. Ji, and all of my committee members, Dr. Wright, Dr. Zourntos, Dr. Coté, and Dr. Ma, for their sincere guidance and consistent support throughout the course of my PhD work.

Finally, I thank my parents for their consistent encouragement and love.

TABLE OF CONTENTS

Page

CHAPTER Page

Page

LIST OF TABLES

Page

LIST OF FIGURES

Page

Page

Page

CHAPTER I

INTRODUCTION

In Magnetic Resonance Imaging (MRI), a number of important clinical applications rely on image phase to provide clinically important information. The partial representative examples include phase-sensitive inversion recovery (PSIR) to extend the dynamic range of image intensity to negative intensity levels (1-2), and Dixon water and fat separation techniques to improve tissue-contrast by suppressing unnecessary fat signals (3-6). These techniques are widely used as the MR contrast-enhancing methods, and Dixon methods providing water-only and fat-only images can be used as a potential and powerful non-invasive tool to study obesity. However, clinical applications of these phase-sensitive contrast-enhancing techniques have been restricted due to three major limitations: (1) difficulty of decomposing spectrally overlapped signals in the chemical-shift domain, (2) limited dynamic range of Dixon techniques, and (3) limited spatio-temporal resolution coming from long imaging time. This work is dedicated to develop more scan-efficient and capable phase-sensitive MR imaging techniques to address aforementioned difficulties, and demonstrate their potential for clinical applications.

I.1 Current Phase-Sensitive Contrast-Enhancing Techniques

In clinical MR imaging, Dixon water/fat separation technique (3-6) and PSIR (1-2) are

---

This dissertation follows the style and format of Magnetic Resonance in Medicine.

two major phase-sensitive contrast-enhancing techniques. Dixon imaging techniques can suppress unnecessary fat signals, therefore improve tissue-contrast as well as eliminate spatial fat-misregistration artifacts generated by chemical-shift of water/fat signals (7-8). Although Dixon techniques were originally devised for fat suppression, they can also be used for obesity and fat quantification in lean tissues (9). Dixon fat suppression techniques have several advantages: they are less susceptible to field-inhomogeneity effects (compared with chemical-shift selective saturation techniques) (10-11), and they can preserve the image SNR of decomposed water-signals (compared with short TI inversion recovery techniques) (12-13). Specifically, using one or more sets of angularly modulated combinations of water and fat signals, the phase error induced by field-inhomogeneity effects can be estimated and compensated in post-processing after image acquisition.

PSIR is another phase-sensitive tissue-contrast enhancing technique, which is dependent on T_1 contrast of signals in the human body (1-2). In the PSIR imaging method, the dynamic range of signal intensity is extended to negative image intensity levels by applying inversion RF pulses at the magnetization preparation part of the pulse sequence. Then, the inverted magnetization is recovered at different rates governed by T_1 relaxation-time during the inversion time (TI) between inversion and excitation RF pulses. This preparation makes it possible to reconstruct the dynamic-range enhanced positive/negative signals. PSIR is useful for many clinical MR applications like pulmonary blood flow evaluation (14), neonate brain imaging (15), and myocardium imaging (1). However, applications of Dixon and PSIR techniques to

clinical routine and the performance of them have been restricted due to three major limitations: (1) incapability of decomposing signals having overlapped resonance frequency bands, (2) limited dynamic range of Dixon images, and (3) long scan time required for both phase-sensitive data acquisition and calibration scans for phase error estimation.

I.2 Difficulty of Decomposing Signals Having Overlapped Resonance Frequency Bands

Dixon techniques depend on chemical-shift. As such, they cannot decompose two signals, if their bands of resonance frequency are overlapped or close to each other. In the Dixon techniques, chemical-shift difference between two signals is directly modulated to relative image-phase difference, and this phase difference is used as the key information to separate two signals (3-6). However, in practice, many MR signals in the human body and body implants have the very similar chemical-shift, i.e., resonance frequency. For example, in MR mammography, suppressing unnecessary fat signals is helpful to identify leaking and ruptures in silicone breast implants (16-17). In April 1992, the Food and Drug Administration found safety issues on silicone breast implants and restricted the use of them (18). Nevertheless, currently 1.3 million women have these devices and many of these implants are antiquated with varying shell design and differing gel formulations (19). Although the life expectancy of these devices is unknown, many scientific reports have warned implant shells slowly degrade during residence in the body (20) to yield rupture rates that can exceed 50% at explantation after 12 years (21). Finding reliable and non-operative methods for detecting breast

implant failure is a challenge in MR mammography. Diagnosing ruptures or leakage is problematic since palpation, assessment of tenderness, and standard breast imaging techniques such as mammography and sonography do not generally provide conclusive evidences (19). It was proven that MRI is more sensitive than competing modalities in the diagnosis of ruptures or leakage of silicone breast implants (19, 22-26). One of the primary reasons for this high sensitivity is because MRI facilitates the acquisition of silicone-specific images in the breast, permitting unequivocal determination of intra- or extracapsular ruptures of silicone-based prostheses. The typical image resolution, which is enough to find ruptures and leaking using MRI, is 0.7 mm × 0.7 cm (19). In this MR application, suppressing unnecessary fat signals improves observation for leaking and ruptures in silicone breast implants. However, Dixon techniques cannot separate silicone signals (4.0 ppm) from fat signals (3.5 ppm) as both have similar chemical-shift (17). Even when resonance frequencies of two signals are separated in theory, spectral bands of these signals can overlap or interfere in practice due to insufficient shimming and field-inhomogeneity. Moreover, interference among multiple spectral components owing to both direct saturation effect and indirect saturation caused by magnetization transfer effects (27) can also limit the performance of Dixon techniques in signal decomposition.

When we try to suppress one of spectrally overlapped signals, suppressing another signal is frequently beneficial to detect and characterize lesions in many clinical MR applications. However, the number of suppressible signals using Dixon techniques is largely restricted to only one, because the output of Dixon technique is

only two signals: water-dominant and fat-dominant signals. For example, in contrast-enhanced MR mammography for patients with breast implants, it is desirable to suppress both fat and implanted silicone signals to capture lesion enhancement patterns in water signals (28). However, multiple signal suppression is hard to achieve only using Dixon techniques. If it is desired, Dixon techniques should be used with other signal-suppression techniques like chemical-shift selective saturation (CHESS) and/or spectral short TI inversion recovery (STIR). CHESS is a fat suppression technique using the combination of frequency-selective RF pulses and spoiler gradients to selectively excite and dephase fat signals before data acquisition in the magnetization preparation part of a pulse sequence (10-11). STIR is another fat suppression technique using specific timing in an inversion recovery pulse sequence so as to suppress the signal from fat (12-13). However, incorporating with CHESS renders the process sensitive to both static (B_0) and RF (B_1) magnetic field-inhomogeneity, potentially resulting in suppressing wrong signals other than target signals to suppress. This can be especially problematic for large FOV and off-isocenter imaging. On the other hand, combining with STIR reduces the dynamic range of residual signals, while waiting for signal null-time of a target signals to suppress (29).

I.3 Limited Dynamic Range of Dixon Images

In fat-suppressed and T_1-weighted MR imaging, it is important to achieve large image-contrast between before and after paramagnetic contrast-agent (e.g., gadolinium dimeglumine) injection to capture lesion enhancement patterns (30). However, in Dixon techniques, intensity of decomposed water signals is restricted to the positive

range from 0 to equilibrium magnetization (M_o). As the result, achievable image-contrast is limited.

In order to improve observation for dynamic tissue-contrast change due to contrast agent uptake, one may consider incorporating multi-point Dixon techniques with PSIR to extend the dynamic range of Dixon images to both positive/negative levels. However, multi-point Dixon techniques are not technically compatible with PSIR, because both rely on the 180º phase difference to identify signal changes between water/fat signals (Dixon) and between positive/negative contrast tissues (PSIR). To address this problem, a new Dixon imaging modality is needed.

I.4 Limited Spatio-Temporal Resolution due to Long Imaging Time

The spatio-temporal resolution of Dixon techniques is limited due to two major reasons: long scan-time to acquire Dixon data acquisition and additional calibration scans for background phase error estimation (31-33), which is necessary for water and fat decomposition in Dixon techniques. In Cartesian MRI, N_{PE} data acquisitions are needed to collect the entire $N_{FE} \times N_{PE}$ data matrix. The total acquisition time can be defined as $N_{Dixon} \times N_{PE} \times TR$, where TR is repetition-time and N_{Dixon} is the number of repeated acquisitions required by the Dixon technique. Spin- or gradient-echo-train can be used to accelerate the acquisition. However, the maximum number of echoes to recall is limited to 16 or 32 due to the dephasing effect. Second, conventional Dixon techniques require additional reference scans to estimate background phase errors for water and fat separation (31-33). For example, if the N_{Calib} number of phase-encoding

lines are used to estimate phase errors, the total imaging time will be $(N_{Dixon} \times N_{PE} + N_{Calib}) \times TR$. For these reasons, it is desirable to develop a scan-efficient and self-calibrating Dixon technique, which can accelerate data acquisition and does not require additional references.

I.5 Dissertation Objective and Organization

The primary objective of this work is to develop novel scan-efficient and contrast-enhanced phase-sensitive MR imaging techniques to overcome three major limitations of current phase-sensitive imaging techniques: (1) difficulty in decomposing signals having overlapped resonance frequency bands, (2) limited dynamic range of Dixon images, and (3) limited spatio-temporal resolution due to long imaging time. Four specific aims were outlined to achieve the objective:

Aim 1: Develop a robust auto-calibrating phase correction method.

Aim 2: Develop a generalized chemical-shift imaging technique incorporating both T_1-contrast and chemical-shift to separate spectrally overlapped signals.

Aim 3: Develop a contrast-enhanced Dixon technique.

Aim 4: Develop an ultra-fast contrast-enhanced single echo acquisition (SEA) imaging technique using phase-sensitive data.

The rest of this dissertation is organized as follows. Chapter II provides the necessary technical background on MR signals, spatial localization, and k-space. Following the fundamental background on MRI, several related imaging methods (CHESS, STIR, Dixon, PSIR and SEA) were discussed. The following four chapters

document the dissertation research corresponding to the four aims listed above.

Aim 1: Chapter III presents a novel auto-calibrating phase correction algorithm based on a rigorous mathematical model and an adaptive Markov random field for background phase error estimation. The developed technique will be used as a robust background phase error estimating method for the rest of work. The primary benefit of using this technique is to improve scan-efficiency by completely eliminating time-consuming additional reference scans for phase correction. Another benefit is that we can prevent errors in the phase error estimation coming from patient's motions between calibration and Dixon data-acquisition scans.

Aim 2: Chapter IV presents a generalized chemical-shift imaging technique incorporating both T_1-contrast and chemical-shift to provide an improved Dixon technique, which can decompose three signals simultaneously, as well as separate chemical species which have similar resonance frequencies.

Aim 3: Chapter V introduces a contrast-enhanced Dixon technique to improve tissue-contrast of Dixon techniques. By integrating a single-point Dixon technique with PSIR, it will show that the extended dynamic range of image intensity can be achievable using the orthogonal phase difference between contrast-enhanced water/fat signals.

Aim 4: Chapter VI discusses an ultra-fast Dixon technique using the SEA imaging technique. We will demonstrate that incorporating a single-point Dixon method with a fully parallel SEA imaging technique can produce water-only and fat-only images with a very fast frame-rate of 1/TR.

Chapter VII summarizes the conclusions and contributions of this work, and describes possible future works.

CHAPTER II

BACKGROUND

Since MRI was introduced in 1972 for the first time (34), it has been used as a powerful and non-invasive imaging modality, providing high-resolution physiological and anatomical information for clinical applications. In this chapter, fundamental MR physics and MRI theories are introduced briefly to understand current limitations on image-contrast and scan-efficiency (35-38). Then, two phase-sensitive contrast-enhancing techniques (Dixon (3) and PSIR (1-2)), a fully parallel imaging method (SEA (39-42)), as well as CHESS (10-11) and STIR (12-13) techniques are discussed as the starting points of the dissertation.

II.1 MR Signals, Spatial Localization, and K-space

In MRI, an ensemble of nuclei of the same type present in an object being imaged is referred to as a nuclear spin system. Nuclei with a nonzero spin generate magnetic fields around them. However, net magnetization of them is approximately zero, as their directions are random in the absence of external magnetic fields due to thermal random motions. When the external magnetic field of strength B_0 is applied in the z-direction, magnetic moment vectors take one of parallel and antiparallel directions of the applied magnetic field, inducing bulk magnetization (M_0) along the direction of B_0. Then, protons can be selectively excited using a radio frequency, which is the same as the resonance frequency (w_0) of interested protons,

$$w_0 = \gamma B_0 \qquad [2.1]$$

where γ is the gyromagnetic ratio of a proton. MRI is primarily dependant on signals from the hydrogen proton ($\gamma = 2\pi \cdot 42.5759$ radians / Tesla) due to its abundance in the soft tissues of the human body. For example, resonance frequencies of hydrogen protons at 1.5 T and 4.7 T are 63.85 MHz and 200.237 MHz, respectively.

A basic spin-echo pulse sequence for MR imaging is shown in Figure 2.1. At t = 0, we apply a combination of a RF excitation pulse and a slice-selection gradient (G_z) to make excitation and spatial localization along the slice selection direction (i.e. z-direction),

$$w(z) = \gamma(B_0 + G_z z) = w_0 + \gamma G_z z \qquad [2.2]$$

By carefully selecting the central frequency (w_0) and bandwidth of the RF pulse, we can selectively excite protons only within a slice at z_0 with the slice-thickness of ST.

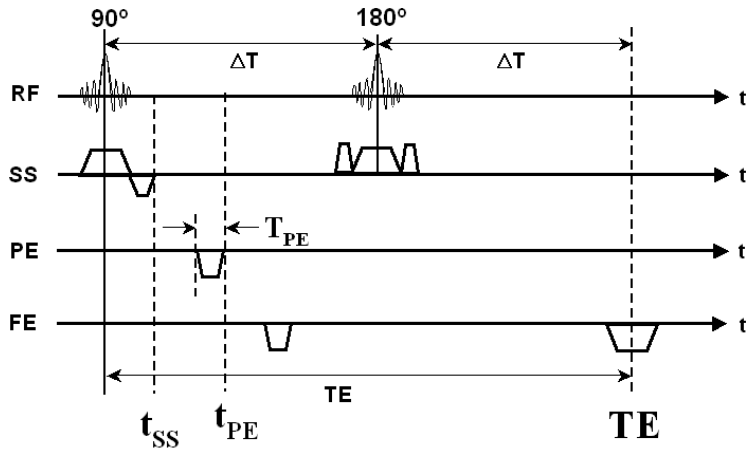

Fig 2.1 A spin-echo pulse sequence for MR imaging. In order to form the $N_{FE} \times N_{PE}$ sized of k-space, the pulse sequence needs to be repeated N_{PE} times.

Then the slice-selected image signals at $t = t_{SS}$ can be expressed,

$$I(x,y) = \int_{z_0 - \frac{ST}{2}}^{z_0 + \frac{ST}{2}} I(x,y,z)dz \qquad [2.3]$$

where I(x, y, z) is the image signal of a voxel at (x, y, z). Following the slice-selection, we apply another G_y gradient during the phase-encoding time of T_{PE} to make linear and spatial frequency variations along the y-direction. At $t = t_{PE}$, the image signal is modulated by the phase-encoding,

$$S(t = t_{PE}) = I(x,y)e^{j\gamma G_y T_{PE} y} = I(x,y)e^{jk_y y} \qquad [2.4]$$

where $k_y = \gamma G_y T_{PE}$. Finally, we apply the G_x gradient to make the third spatial localization along the x-direction. Then, two-dimensional k-space information is acquired at an echo-time (TE), which is 2-D Fourier transform of the image in the field-of-view (FOV),

$$S(k_x,k_y) = \iint_{FOV} I(x,y)e^{jk_x x}e^{jk_y y}dxdy \qquad [2.5]$$

where $k_x = \gamma G_x t$.

II.2 Chemical-Shift Selective Saturation (CHESS)

CHESS is a fat suppression technique using the resonance frequency difference between water and fat signals (10-11). Figure 2.2 illustrates the pulse sequence diagram of CHESS based on a spin-echo pulse sequence. In the magnetization preparation part of the pulse sequence, the combination of a frequency-selective RF pulse and spoiler gradients are used to selectively excite and dephase fat signals. Then,

regular spin echo pulse sequences are played to acquire water-only signals.

II.3 Short TI Inversion Recovery (STIR)

STIR is another fat suppression technique using specific timing in an inversion recovery pulse sequence so as to suppress signals from fat (12-13). Figure 2.3 illustrates the pulse sequence diagram of STIR based on a spin-echo pulse sequence.

In the magnetization preparation part of a pulse sequence, an inversion RF pulse is used to invert longitudinal magnetization of water and fat signals. Then, longitudinal magnetizations of fat and water signals are recovered at different rates, governed by unique T_1 relaxation time. When the longitudinal magnetization of fat signals is voided, regular spin-echo pulse sequences are applied to acquire water-only signals.

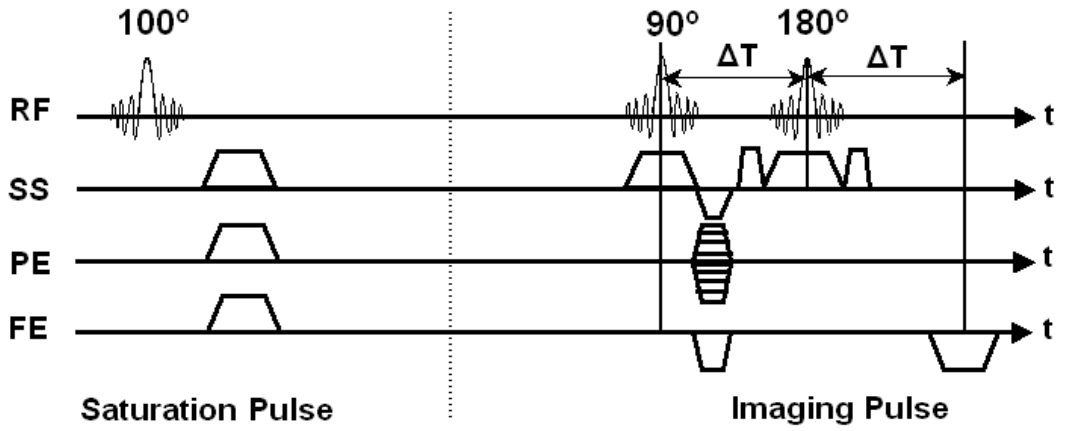

Fig 2.2 The pulse sequence diagram of CHESS using the combination of frequency-selective RF pulses and spoiler gradients to selectively excite and dephase fat signals.

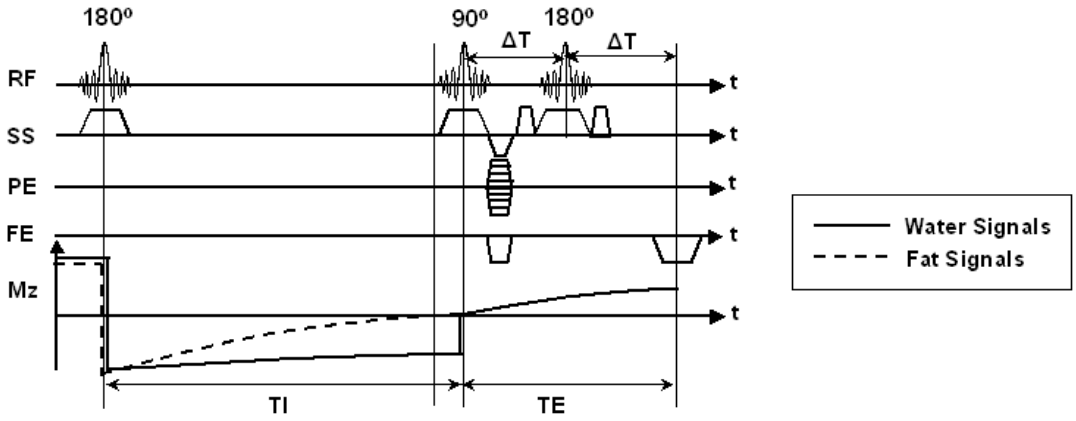

Fig 2.3 The pulse sequence diagram of STIR using specific timing in an inversion recovery pulse sequence to suppress fat signals.

II.4 Dixon Water/Fat Imaging

Dixon techniques can improve tissue contrast by suppressing unnecessary fat signals (3). Even in a perfectly homogeneous static magnetic field, local fields vary at the molecular level. As the result, resonance frequency of protons in lipid-based compound (containing CH_2 and CH_3) is shifted to a lower frequency compared with protons in water (H_2O). Figure 2.4 illustrates the chemical-shift phenomenon between water and fat signals. The difference of resonance frequencies of water and fat signals (Δf) are defined as,

$$\Delta f = -\sigma_{fw} f_w \qquad [2.6]$$

where σ_{fw} is chemical-shift between water and fat signals (= 3.5 ppm), and f_w is the Larmor frequency of water protons. For example, at 1.5 T static magnetic field, the resonance frequency difference between water and fat signals is 224 Hz, and resonance frequencies of water and fat signals are 63,870,000 Hz and 62,869,776 Hz, respectively.

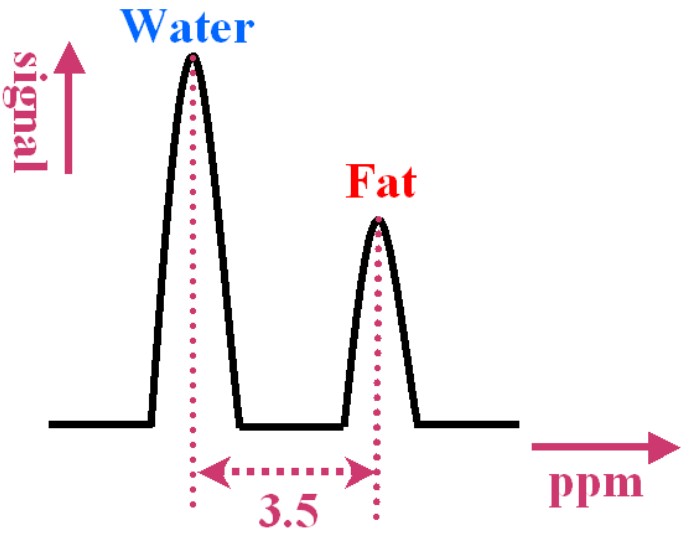

Fig 2.4 Chemical-shift between water and fat signals. Due to local field variation in the molecular level, the resonance frequency of protons in fat signals (3.5 ppm) is shifted to the lower frequency compared with that of protons in water signals (0 ppm).

A spin-echo based Dixon pulse sequence is illustrated in Figure 2.5. At the regular echo time at t = 2ΔT, both water and fat signals are inphase. However, the chemical-shift produces linear phase differences between water and fat signals periodically. By shifting data acquisition window by ΔT_{shift}, we can acquire angularly modulated water (W) and fat (F) image signals as follows,

$$I(x,y) = (W(x,y) + F(x,y)e^{j2\pi\Delta f\Delta T_{shift}})e^{j\theta(x,y)} \quad [2.7]$$

where θ(x, y) is ubiquitous and user-uncontrollable spatially-varying phase errors due to off-resonance frequency-shift induced by B_0 inhomogeneity, varying susceptibilities of different tissues, eddy currents, and/or complex coil sensitivity.

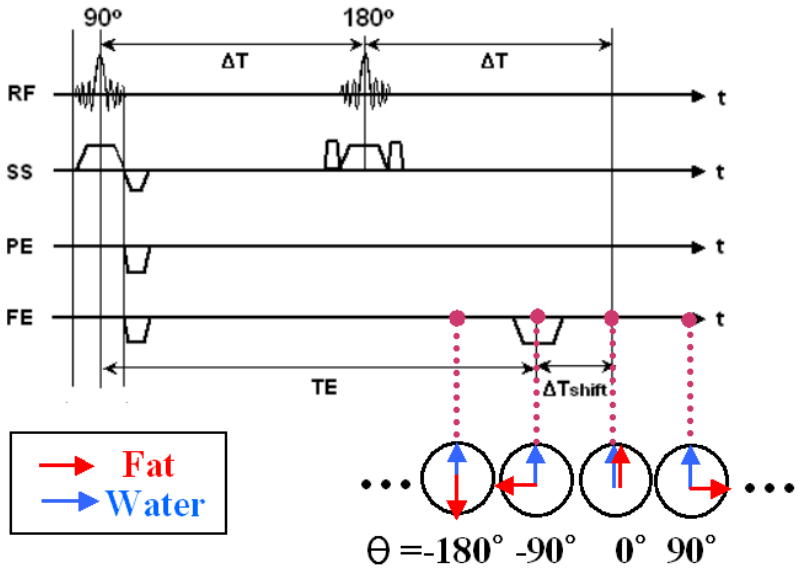

Fig 2.5 A spin-echo based Dixon pulse sequence. The resonance frequency difference between water and fat signals produces linear phase difference between them periodically. By shifting data acquisition window, we can acquire angularly modulated water and fat image signals.

II.4.1 Two-Point Dixon Technique

Depending on the number images used for water and fat decomposition, Dixon techniques can be categorized to three groups: three-point (4-6), two-point (3) and single-point Dixon techniques (43). Three-point Dixon technique can achieve the highest SNR among three techniques. However, clinical applications of the three-point Dixon technique have been limited due to huge data acquisition time. In the case of two-point Dixon techniques, ΔT_{shift} is selected to have in-phase ($I_{in}(x,y)$) and out-of-phase ($I_{out}(x,y)$) images as such,

$$I_{in}(x,y) = (W(x,y) + F(x,y))e^{j\varphi(x,y)} \qquad [2.8]$$

$$I_{out}(x,y) = (W(x,y) - F(x,y))e^{j(\varphi(x,y) + \theta(x,y))} \quad [2.9]$$

where $\varphi(x,y)$ is the phase error of an in-phase image, and $\theta(x,y)$ is the additional phase error due to B_0 field inhomogeneity accumulated during the time between in-phase and out-of-phase signal acquisitions (44). After $\varphi(x,y)$ is removed from the both signals, we get modified in-phase and out-of-phase signals,

$$I'_{in}(x,y) = I_{in}(x,y)e^{-j\varphi(x,y)} = W(x,y) + F(x,y) \quad [2.10]$$

$$I'_{out}(x,y) = I_{out}(x,y)e^{-j\varphi(x,y)} = (W(x,y) - F(x,y))e^{j\theta(x,y)} \quad [2.11]$$

The estimation for $\theta(x,y)$ is not simple, but an important issue in phase-sensitive MR imaging techniques like PSIR and Dixon techniques. Currently available techniques typically rely on several sets of reference images for the estimation (31-33). However, these methods have several limitations in performance. First, phase error estimation using additional calibration scans frequently fails due to patient's motions and flows in the human body, which can induce significant errors in the image phase between calibration and Dixon imaging scans. Second, time-consuming additional scans may not be compatible with many MR applications requiring high frame-rates. To address these problems, a robust self-calibrating background phase error estimating algorithm is developed in Chapter III. If we assume $\theta(x,y)$ has been estimated, water and fat signals can be simply decomposed using arithmetic operations as such,

$$W(x,y) = 0.5(I'_{in}(x,y) + I'_{out}(x,y)e^{-j\theta(x,y)}) \quad [2.12]$$

$$F(x,y) = 0.5(I'_{in}(x,y) - I'_{out}(x,y)e^{-j\theta(x,y)}) \quad [2.13]$$

II.4.2 Single-Point Dixon Technique Using Arbitrary Echo-Time

The two-point Dixon technique was discussed above. However, long scan-time required to acquire both in-phase and out-of-phase images may not be compatible with fast MR imaging applications. In this case, the single-point Dixon technique using arbitrary echo-time (45) can be an alternative solution. In the technique, water and fat signals are modulated to have arbitrary phase difference (only excluding 0° and 180°) as such,

$$I(x,y) = (W(x,y) + F(x,y)e^{j2\pi\Delta f\Delta T_{shift}})e^{j\theta(x,y)} \quad [2.14]$$

where ΔT_{shift} is the shifted echo-time in Figure 2.5, Δf is resonance frequency difference between water and fat signals, and $\theta(x,y)$ is the phase errors induced by static magnetic field inhomogeneity and other system imperfections. If we assume $\theta(x,y)$ is known, the phase corrected signal can be acquired as such,

$$I'(x,y) = I(x,y)e^{-j\theta(x,y)} = W(x,y) + F(x,y)e^{j\varphi} \quad [2.15]$$

where $\varphi = 2\pi\Delta f\Delta T_{shift}$. Then, fat and water signals can be simply decomposed as follows,

$$F(x,y) = Im\{I'(x,y)\}/\sin\varphi \quad [2.16]$$

$$W(x,y) = Re\{I'(x,y)\} - F(x,y)\cos\varphi \quad [2.17]$$

where $Re\{\cdot\}$ and $Im\{\cdot\}$ are operators to get real and imaginary parts of complex signals, for each.

II.5 Phase-Sensitive Inversion Recovery (PSIR) Imaging

PSIR is another phase-sensitive tissue-contrast enhancing method, which is dependent on T_1 contrast of signals in the human body. PSIR can improve tissue-contrast by extending the dynamic range of image intensity to negative intensity levels (1-2). Figure 2.6 illustrates a PSIR pulse sequence diagram. In the magnetization preparation part of the pulse sequence, the direction of net magnetization is inverted using a 180° RF pulse. Afterwards, the inverted magnetization is recovered at the different rates governed by different T_1 relaxation-time for each signal during the inversion time (TI) between inversion and excitation RF pulses. Then, the acquired signals (S) at an echo-time can be expressed as follows,

$$S(x,y) = I_{PSIR}(x,y)e^{j\theta(x,y)} \qquad [2.18]$$

where I_{PSIR} is the dynamic-range enhanced positive/negative signals and $\theta(x,y)$ is the phase errors induced by static magnetic field inhomogeneity and other system

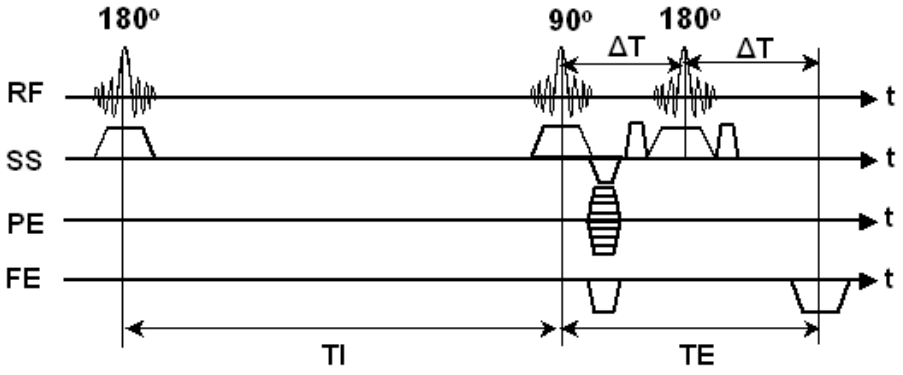

Fig 2.6 A phase-sensitive inversion recovery pulse sequence. Inversion time (TI) is carefully selected to produce both positive and negative signals for interested signals.

imperfections. Once the phase error term is known, the contrast-enhanced PSIR signals can be reconstructed simply by,

$$I_{PSIR}(x,y) = \mathrm{Re}\{S(x,y)e^{-j\theta(x,y)}\} \quad [2.19]$$

If phase error estimation is not accurate, phase-corrected signals (i.e. $S(x,y)e^{-j\theta(x,y)}$) may not be real, but complex signals. To alleviate this issue, the phase corrected signals were approximated by using the $\mathrm{Re}\{\cdot\}$ operator.

II.6 Single-Echo Acquisition (SEA) Imaging

The SEA imaging technique is a fully parallel imaging method, which can acquire a 2-D image with simultaneously acquired echoes within TR (39-42). In SEA imaging, time-consuming multiple phase-encoding steps are replaced by extremely localized coil sensitivity in the level of image pixel size (i.e. Δy). The SEA signal (D) acquired from the c-th channel can be expressed as follows,

$$D_c(k_x) = \iint I(x,y)\left|S_c(x,y)\right| e^{j\theta_c(x,y)} e^{-jk_x x}\,dx\,dy \quad [2.20]$$

where $|\cdot|$ is a magnitude operator, $I(x, y)$ is the image signal, $S_c(x, y)$ is the coil sensitivity of the c-th channel, and $\theta_c(x, y)$ is the phase error of the c-th channel induced by various possible sources such as B_0 field inhomogeneity, varying susceptibilities of different tissues, eddy currents, and complex coil sensitivity. In SEA imaging, the coil-sensitivity is very localized along the y-direction in the level of the pixel size. Thus, the above equation can be simplified to

$$D_c(k_x) \approx \int I(x,y_c)\left|S_c(x,y)\right| e^{j\theta_c(x,y_c)} e^{-jk_x x}\,dx \quad [2.21]$$

where y_c is the central location of the c-th coil along y-direction. After 1-D inverse

Fourier transform of $D_c(k_x)$, an image line at y_c can be formed as such,

$$\hat{I}_c(x) \approx \left| I_c(x) e^{j\theta_c(x)} \right| \qquad [2.22]$$

where $I_c(x) = I(x,y_c) \cdot \left| S_c(x,y_c) \right|$ which is the sensitivity-weighted image signals. Then, a complex 2-D SEA image can be reconstructed by stacking all 64 image lines $I_c(x)$, c = 1, 2, …, 64, together.

CHAPTER III

PHASE CORRECTION

USING ADAPTIVE MARKOV RANDOM FIELD MODEL

Phase correction is an important issue in phase-sensitive MR imaging as discussed in Chapter II. Some of currently available techniques require time consuming additional reference scans for phase estimation (31-33, 46-47). However, these methods have several limitations. First, estimation methods using additional calibration scans frequently fail due to patient's motions and flow artifacts. Second, acquiring additional scans is time-consuming and may not be compatible with MR applications requiring high frame-rates.

In this research, we developed a novel auto-calibrating phase correction algorithm based on a rigorous mathematical model and an adaptive Markov random field for background phase error estimation. This model adaptively selects the size of neighboring references depending on the degree of smoothness of the phase map. For example, the relatively smaller number of neighboring references is used for local regions with rapid phase variations in order to reduce errors in the estimation.

III.1 Methods

III.1.1 Adaptive Markov Random Field Model

A Markov chain (48) is a sequence of random variables with the Markov property, namely that conditional distribution in a Markov chain is only dependent on the

neighboring states,

$$P(X_n = x_n | X_k = x_k, k^1 n) = P(X_n = x_n | X_{n-k} = x_{n-k,}\ k = -p,...-1, 1,...,p) \qquad [3.1]$$

where n, k and p are integer. To define a Markov random field (MRF) (49), let S be a set of rectangular lattice of the $N_x \times N_y$ sized of an image. Then, S is defined as,

$$S = \{(x,y) \,|\, 1 \le x \le N_x, 1 \le y \le N_y\} \qquad [3.2]$$

The points in S are called sites. A neighborhood system in S can be defined as,

$$N(x,y) = \{(x',y') \in S, (x'-x)^2 + (y'-y)^2 \le r^2, (x,y) \ne (x',y')\} \qquad [3.3]$$

This means: (1) a site is not neighboring to itself, and (2) the neighboring relationship is mutual. A MRF of function I(x, y), i.e., complex mage, defined on S can be represented as,

$$P\{I(x,y)|\{I(x',y'), (x',y') \in S, (x',y') \ne (x,y)\}\}$$

$$= P\{I(x,y)|\{I(x',y'), (x',y') \in N(x,y), (x',y') \ne (x,y)\}\} \qquad [3.4]$$

For phase estimation, we model the background phase error $\Theta = \{\theta(x,y)|(x,y) \in S\}$ as MRF. The goal is to use the model to estimate Θ from the observed phase $\Phi = \{\varphi(x,y)|(x,y) \in S\}$ of the complex image.

In the MRF theory, the phase error can be estimated by maximizing a posteriori (MAP) estimator,

$$\hat{\Theta} = \arg\max_{\Phi} P(\Theta \,|\, \Phi) \qquad [3.5]$$

$$= \arg\max_{\Phi} P(\Phi \,|\, \Theta) P(\Theta) \qquad [3.6]$$

where $P(\Theta|\Phi)$ and $P(\Theta)$ are the posterior and prior probabilities, and $P(\Phi|\Theta)$ is the

likelihood function (50-52). To solve the MRF problem, we define the likelihood function ($P(\Phi|\Theta)$) (53) and the *prior* probability ($P(\Theta)$) according to the Hammersley-Clifford theorem (54) as follows,

$$P(\Phi|\Theta) = \delta[\Phi - w(\Theta)] \qquad [3.7]$$

$$P(\Theta) \propto \exp(-\frac{\sum_{(x,y)\in S} V(\theta(x,y))}{T}) \qquad [3.8]$$

where δ is the Dirac delta function, w is a wrapping operator, V is a potential function, and T is a normalization factor chosen to be unity in the dissertation. Given the Makovian properties, the MAP estimator in Eq. [3.6] can be represented as (53),

$$\hat{\Theta} = \arg\max_{\Phi}\{\prod_{(x,y)\in S}\prod_{(x',y')\in S}\delta[\varphi(x',y')-w(\theta(x',y'))]\cdot\exp(-\sum_{(x',y')\in S}V(\theta(x',y')))\} \qquad [3.9]$$

In this dissertation, the $w(\cdot)$ is operator is represented as,

$$\varphi(x,y) = \theta(x,y) + p(x,y) \qquad [3.10]$$

where $\{P = p(x,y)|(x,y)\in S\}$ is a field, which takes possibilities depending on applications. In PSIR or two-point Dixon images, p(x, y) can be either 0 or π depending on the polarity of signal intensity at (x, y). We define the potential function as,

$$V(\Theta) = \sum_{(x,y)\in S}\sum_{(x',y')\in S}\left|\angle[I(x,y)\cdot I^{*}(x',y')]\right|\frac{\left|I(x',y')\right|}{G_x(x',y')\cdot G_y(x',y')} \qquad [3.11]$$

where * indicates the complex conjugate operator, and $G_x(\cdot)$ and $G_y(\cdot)$ are angular gradients along x and y directions,

$$G_x = \left|\angle[I(x',y')\cdot I^{*}(x'-1,y')]\right| \qquad [3.12]$$

$$G_y = \left| \angle [I(x',y') \cdot I^*(x',y'-1)] \right| \qquad [3.13]$$

This potential function gives more weighting on pixels with the higher SNR to improve robustness in decision-making, assuming that noisy pixels can be characterized with relatively low signal intensities and higher degrees of phase gradients.

Then, maximizing a posteriori (MAP) estimator can be achieve by,

$$\Theta_{opt} = \arg \min_{\Phi} V(\Theta) \qquad [3.14]$$

where $\Theta = \Phi + P$ (53). Specifically, if we assume p(x, y) has two binary states (i.e. either 0 or p_0), the observed phase of a complex image can be either $\theta(x, y)$ or $\theta(x, y) + p_0$. Then, the background phase error ($\varphi(x, y)$) of a pixel can be estimated by comparing two possible values of potential functions using smooth phase constrains,

$$\text{If } \varepsilon(\Theta) < \varepsilon(\Theta - p_0), \text{ then } \Phi = \Theta \qquad [3.15]$$

$$\text{If } \varepsilon(\Theta) > \varepsilon(\Theta - p_0), \text{ then } \Phi = \Theta - p_0 \qquad [3.16]$$

III.1.2 Optimization Using Adaptive Region-Growing Algorithm

The MRF models the true phase function as a smooth function, and parameters in the model are determined by MAP. The optimal solutions for parameters can be found using either a global or a local optimizing algorithm. Generally, numerical complexity for global optimizing algorithm is high even for moderately sized images. For example, the brutal search algorithm based on global optimum requires testing all the $2^{N_x \times N_y}$ possibilities for the $N_x \times N_y$ sized of an image (54). Between two optimizing

methods, local optimizing algorithms such as region-growing algorithms have been widely used, as they are faster. For example, the region-growing algorithm is a robust local optimizing method based on highest confidence first (HCF) criterion (54). In this technique, the estimation of the Θ field is achieved by local adjustment, but the adjustment is performed on the pixels with high SNR first. Error propagation during the process of phase estimation is reduced by performing phase correction in higher SNR regions first to build more reliable references for phase error estimation. In these methods, the neighborhood definition is typically fixed to be a square, assuming the smoothness over the whole image is the same. However, universal smooth phase constraint may not be valid in many clinical MR applications like whole body imaging and large FOV imaging, which are sensitive to inhomogeneity and local susceptibility due to body cavities. In this case, MRF models need to be dynamically tuned to achieve the desirable phase correction outcome.

III.1.2.1 Initial-Seed Selection

After a complex image, I(x, y), is reconstructed from k-space data, $S(k_x, k_y)$, using 2-D inverse Fourier transform, x and y directional gradients, $G_x(x, y)$ and $G_y(x, y)$, are calculated using Eqs. [3.12] and [3.13]. An initial seed, $I(x_0, y_0)$, is selected form a pixel with the minimum phase gradient in both horizontal and vertical directions (44) as follows,

$$I(x_o,y_o) = \{I(x,y) \mid G_x(x_o,y_o) = \min_{1\le x\le N_x}(G_x(x,y)), G_y(x_o,y_o) = \min_{1\le y\le N_y}(G_y(x,y))\} \quad [3.17]$$

III.1.2.2 Selection of a Sequence for Phase Correction

Starting from the initial seed, $I(x_0, y_0)$, the sequence of phase correction is followed by one of contingent neighboring pixels, which has the smallest phase difference from a currently processing pixel (44). Specifically, after the (n-1)-th pixel is processed, the n-th pixel is selected as follows,

$$(x_{n,}y_n) = \{(x_{p,}y_p)|G_x(x_{p,}y_p) = \min_{(x_k,y_k)\in N(x_{n-1},y_{n-1})} G_x(x_{k,}y_k), G_y(x_{p,}y_p) = \min_{(x_k,y_k)\in N(x_{n-1},y_{n-1})} G_y(x_{k,}y_k)\} \quad [3.18]$$

These two rules in Eqs. [3.17] and [3.18] help to build more reliable neighboring references for phase correction in homogeneous regions (i.e. non-transition region between two chemical species) early. In other words, testing boundary regions between two different chemical species, which would happen relatively later and which spatially reside around homogeneous regions, can fully utilize reliable references already built on non-transition regions in early time, in the sense that only predetermined neighboring priori information will be used as the reference for the following phase correction.

III.1.2.3 Adaptive Selection for Neighborhood of MRF

Phase error estimation using the MRF depends on spatially smooth phase constrains (53-54). If the degree of local phase variation is small, incorporating a large neighborhood frequently reduces errors in decision-making statistically. However, when phase changes rapidly, using large neighborhood will introduce undesirable error in the estimation. In this case, it is desirable to use only smaller neighborhood for background phase estimation. Figure 3.1 illustrates the adaptively selected neighboring

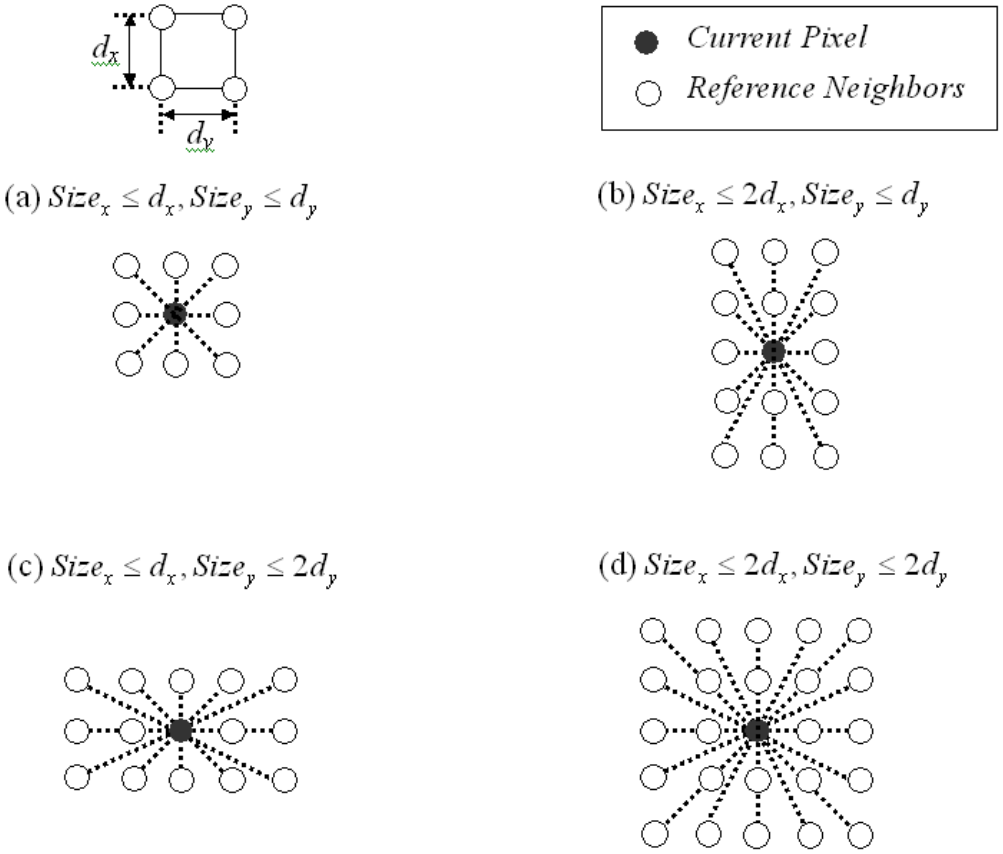

Fig 3.1 Examples of adaptively selected neighborhood in the adaptive Markov random field model. Sizes of neighboring references were selected independently using x and y directional gradients.

references in the MRF model. Specifically, the sizes of neighboring references were selected separately using x and y directional gradients of I(x,y),

$$\text{Reference Size}_x = \frac{xx}{G_x(x,y)} \qquad [3.19]$$

$$\text{Reference Size}_y = \frac{xy}{G_y(x,y)} \qquad [3.20]$$

III.1.2.4 Background Phase Error Estimation

After neighboring references are selected adaptively, $\theta(x, y)$ of a current pixel is estimated using the potential function defined in Eq. [3.11]. Specifically, if $s(x, y)$ has two binary states (i.e. either 0 or s_0), two possible values of potential functions are compared to estimate the background phase error ($\varphi(x,y)$) using Eqs. [3.15] and [3.16]. When we compose neighboring references, only previously phase corrected neighbors are incorporated in decision-making in order to be fully dependent on prior information for phase estimation.

III.1.3 Generalized N-nary Adaptive Markov Random Field Model

In the adaptive MRF model introduced in Section III.1.1, we assumed $s(x, y)$ has two binary states (i.e. either 0 or s_0). If $s(x, y)$ has N possible states such as $\{s_i | i \text{ is integer}, 1 \le i \le N\}$, the observed phase of a complex image also have N possible values (i.e. $\theta(x, y) + s_i$). Then, the proposed MRF model can be extended to estimate background phase error. The region-growing can be achieved by comparing N possible values of potential functions at each current site, and selecting the optimal s_i satisfies,

$$\varepsilon(\Theta - s_i) < \varepsilon(\Theta - s_j), i \neq j : \Phi = \Theta - s_i \qquad [3.21]$$

The extended N-nary adaptive MRF model will be used for the background phase error estimation in Chapter IV and V.

III.2 Experiments

III.2.1 Real Experiment

In vivo human brain images were acquired on a GE Signa 3.0 Tesla whole-body MR scanner (GE Healthcare, Waukesha, WI) using an inversion recovery fast spin-echo pulse sequence and an eight-channel phased-array head coil (MRI Devices, Gainesville, FL). The scan parameters used were as follows: TR / TE / TI = 2 s / 8.4 ms / 450 ms, FOV = 20 cm × 20 cm, number of slice = 7, slice thickness (ST) = 4 mm, receiver bandwidth = 31.25 kHz, image matrix = 256 × 256, and scan-time = 9 minutes and 18 seconds. For evaluation, the ground truth phase information was acquired using the same pulse sequence and scan parameters, but without inversion RF pulses.

Background phase errors were estimated using the proposed method. To compare the estimated phase with ground-truth, mean angular error (MAE) (55) was defined as,

$$\mathrm{MAE} = \frac{1}{\mathrm{N}} \sum_{(x,y)\in \mathrm{ROI}} \left| \arg\{ \mathrm{I}_{\mathrm{Estimate}} \cdot \mathrm{I}^{*}_{\mathrm{Ground\text{-}Truth}} \} \right| \qquad [3.22]$$

where N is the number of pixels in ROI, $\mathrm{I}_{\mathrm{Estimate}}$ is a complex image including the estimated phase information using the proposed technique, and $\mathrm{I}_{\mathrm{Ground\text{-}Truth}}$ is a complex image including phase reference. To demonstrate the effect of using the adaptively selected neighborhood in MRF model, MAE was evaluated for estimated phase errors using fixed reference sizes of 5 × 5, 7 × 7, 9 × 9, 11 × 11, 13 × 13, 15 × 15, 17 × 17, 19 × 19, and 21 × 21.

III.2.2 Computer Simulations

The accuracy of decomposing water and fat signals using the developed technique was evaluated in computer simulations. After water and fat maps are defined, a set of complex single-point Dixon images was produced to have 90° phase difference between water and fat signals, and various magnitude ratios between water and fat signal intensities. The intensity of water signal was fixed to 1.0 and the magnitudes of fat signals were varied from 0.5 to 6.5 with the step size of 0.5. Spatially varying image phase is simulated using a linear function with the rate of 10 degrees per pixel in both image directions. Complex Gaussian random noises were added to the k-space in order to make several SNR conditions (15, 20, 25, and 30 dB) for each phantom image.

Background phase errors of the simulated single-point Dixon datasets were estimated using the proposed MRF method. After phase error is removed, water-only and fat-only images were decomposed using real and imaginary parts of complex signals, as discussed in Section II.4.2. The accuracy of decomposed fat signals was evaluated using the error of fat signal separation defined as,

$$\text{Error of Fat Signal Separation (\%)} = \frac{100\left|\left|\text{Fat Signal}_{\text{Ground-Truth}}\right| - \left|\text{Fat Signal}_{\text{Acquired}}\right|\right|}{\left|\text{Fat Signal}_{\text{Ground-Truth}}\right|} \quad [3.23]$$

The experiments were repeated 100 times, each with randomly selected different initial seeds.

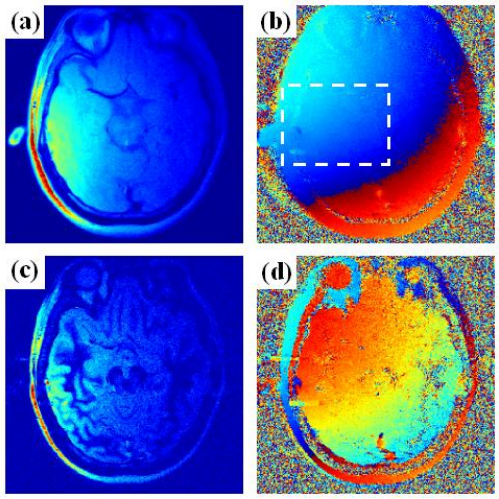

Fig 3.2 Acquired brain images. (a) magnitude and (b) phase images of the reference, and (c) magnitude and (d) phase images from PSIR reconstruction. The rectangle in Fig 3.2 (b) indicates the selected ROI for the MAE evaluation.

III.3 Results

III.3.1 Real Experiment

Figure 3.2 shows the reference magnitude (Figure 3.2 (a)) and phase images (Figure 3.2 (b)) acquired. PSIR magnitude and phase images are shown in Figure 3.2 (c) and (d), respectively. Discontinuous phase information in Figure 3.2 (d) was induced by the intrinsic phase (π) between positive and negative polarities of signal intensities.

Figure 3.3 (a) illustrates the estimated phase map reconstructed after background phase error estimation using the proposed technique. The error map between the estimated phase map and a phase ground-truth in Figure 3.2 (b) was shown in Figure 3.3 (b). The MAE was 0.0571. The rectangle shown in Figure 3.2 (b) indicates the selected ROI for MAE measurement.

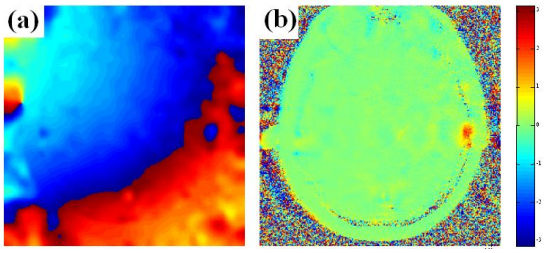

Fig 3.3 Phase correction results using the proposed technique. (a) estimated phase map, and (b) error map between the estimated phase using the proposed technique and a phase reference in Fig 3.2 (b).

The robustness of the proposed adaptive Markov random field model was tested by comparing to the same technique, but with fixed sizes of neighbored sites. Figure 3.4 demonstrates that, with the fixed neighboring size, the best MAE region-growing algorithm could achieve was 0.064. The MAE from the proposed method using the adaptive MRF model was 0.0571. The improvement was 11%.

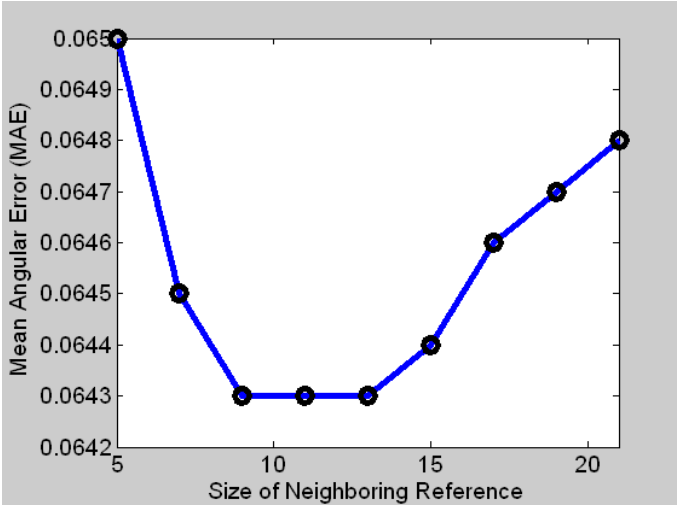

Fig 3.4 Mean angular error (MAE) of estimated background phase errors using the proposed technique, but with fixed sizes of neighborhood from 5×5 to 21×21.

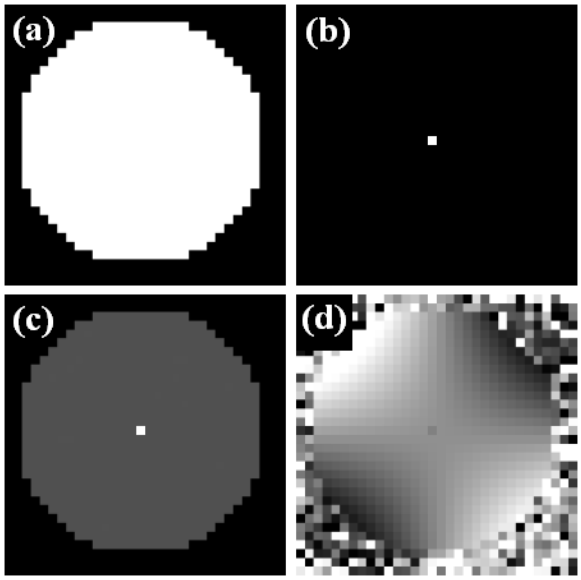

Fig 3.5 Images from computer simulations to test the capability of decomposing water and fat signals using the developed technique. (a) a water map, (b) a fat map, (c) a magnitude image simulating single-point Dixon data, and (d) a phase map having the orthogonal phase difference between water and fat signals.

III.3.2 Computer Simulations

The accuracy of decomposing water and fat signals using the developed technique was tested in computer simulations. Figure 3.5 illustrates images used for the computer simulation. Water and fat maps are defined as shown in Figure 3.5 (a) and (b), respectively. A set of complex single-point Dixon images (Figure 3.5 (c) magnitude and (d) phase map) was produced to have 90° phase difference between water and fat signals, and various magnitude ratios between water and fat signal intensities.

Each of simulated single-point Dixon images was processed to estimate and eliminate phase errors using the proposed technique. The sensitivity of detecting intrinsic phase difference (i.e. 90°) between water and fat signals was evaluated by

measuring the error of fat signal separation as defined in Eq. [3.23]. Figure 3.6 shows measured errors of fat signal separation for various magnitude ratios of mixed water and fat signal intensities in four SNR levels from 15 dB to 30 dB. It was demonstrated that the proposed technique could decompose water and fat signals within the fat signal separation error of 1%, even when the intensity of fat signals is only 50% of water signals at the SNR level of 30 dB.

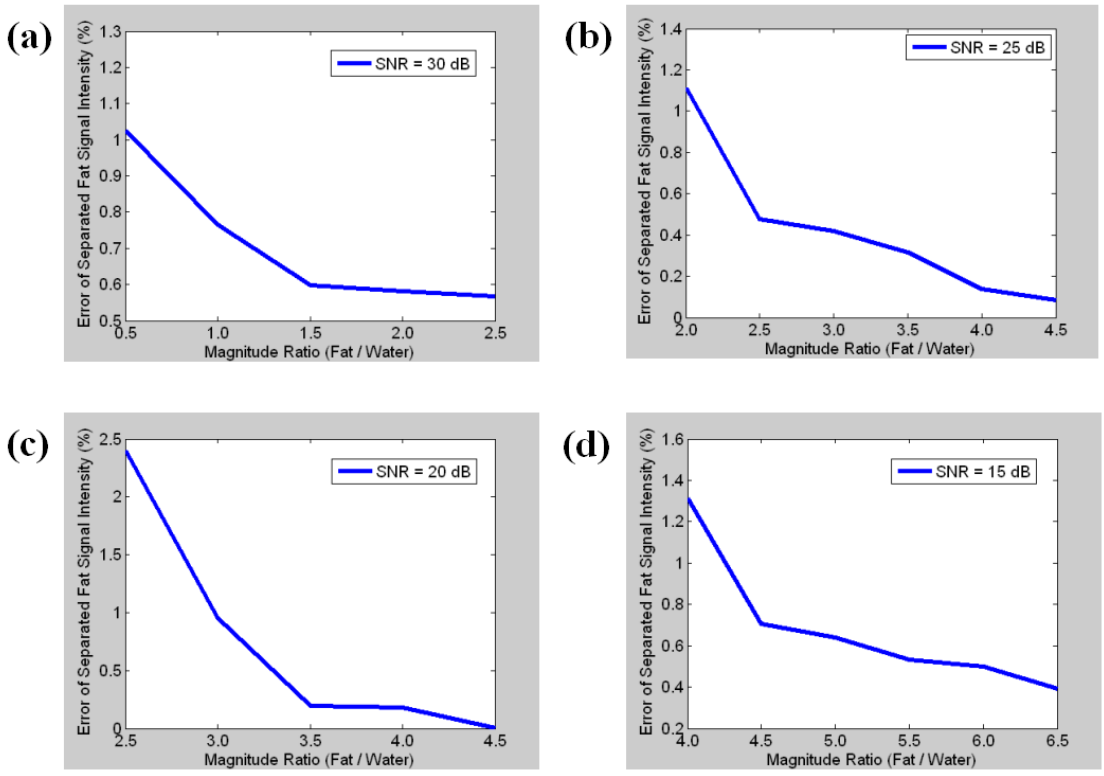

Fig 3.6 Separation errors vs. magnitude ratios of mixed water/fat signals under different SNR levels of (a) 30 dB, (b) 25 dB, (c) 20 dB, and (d) 15 dB. Each result is from the average of 100 trials.

III.4 Discussion

In this research, we developed a novel auto-calibrating phase correction algorithm based on a rigorous mathematical model and an adaptive Markov random field for background phase error estimation. This model adaptively selects the size of neighboring references depending on the degree of smoothness of the phase map. In vivo experiment performed on a clinical scanner using PSIR brain images demonstrated the proposed technique could estimate phase errors successfully only using a single data acquisition. The MAE was 0.0571. The proposed adaptive Markov random field model can robustly estimate the phase using neighborhood sizes from 5×5 to 21×21, but MAE will be reduced by 11%. Finally, the capability of decomposing water and fat signals using the developed technique was tested in computer simulations. The result showed the proposed technique could decompose water and fat signals within the fat signal decomposition error of 1%, even when the intensity of fat signals is only 50% of water signals, and SNR was 30 dB. A general concept of extending the developed technique to a generalized *N*-nary Adaptive Markov Random Field Model was discussed in Section III.1.3.

There are latent issues associated with the proposed technique. If tissues are disconnected with large signal gaps, the signal-void between two isolated tissues prevents successful region-growing over the area (56). In turn, this will introduce ambiguity in determining water and fat signals, resulting in local water and fat misidentification. This problem can be solved by extending the 2-D region-growing algorithm to the 3-D domain. The 3-D region-growing algorithm does not suffer from

local water and fat misidentification problem due to signal-voids, as human extremities and inner organs are interconnected in the 3-D domain. In some cases, this issue may be alleviated by padding physical structures such as water bags between two isolated ROI regions.

CHAPTER IV

GENERALIZED CHEMICAL-SHIFT IMAGING TECHNIQUE INCORPORATING BOTH T_1-CONTRAST AND CHEMICAL-SHIFT

In Dixon techniques, the resonance frequency difference (i.e. chemical-shift) between two signals is directly modulated to relative image-phase difference, and this phase difference is used as the key information to separate two signals (3). As the result, conventional Dixon techniques cannot decompose two signals if their bands of resonance frequency are overlapped or close to each other. However, in practice, many MR signals in the human body and body implants have the very similar chemical-shift, i.e., resonance frequency. For example, in MR mammography, suppressing unnecessary fat signals is helpful to identify leaking and ruptures in silicone breast implants (16-17). In April 1992, the Food and Drug Administration found safety issues on silicone breast implants and restricted the use of them (18). Nevertheless, currently 1.3 million women have these devices and many of these implants are antiquated with varying shell design and differing gel formulations (19). Although the life expectancy of these devices is unknown, many scientific reports have warned implant shells slowly degrade during residence in the body (20) to yield rupture rates that can exceed 50% at explantation after 12 years (21). Finding reliable and nonoperative methods for detecting breast implant failure is a challenge in MR mammography. Diagnosing ruptures or leakage is problematic since palpation, assessment of tenderness, and standard breast imaging techniques such as mammography and sonography do not

generally provide conclusive evidence (19). It was proven that MRI is more sensitive than competing modalities in the diagnosis of ruptures or leakage of silicone breast implants (19, 22-26). One of the primary reasons for this high sensitivity is because MRI facilitates the acquisition of silicone-specific images in the breast, permitting unequivocal determination of intra- or extracapsular ruptures of silicone-based prostheses. The typical image resolution, which is enough to find ruptures and leaking using MRI, is 0.7 mm × 0.7 cm (19). In this MR application, suppressing unnecessary fat signals improves observation for leaking and ruptures in silicone breast implants. In order to improve observable ability to find ruptures and leaking in the silicone breast implants, fat suppression has been achieved by using CHESS and/or STIR. CHESS is a fat suppression technique using the combination of frequency-selective RF pulses and spoiler gradients to selectively excite and diphase fat signals before data acquisition in the magnetization preparation part of a pulse sequence (10-11). STIR is another fat suppression technique using specific timing in an inversion recovery pulse sequence so as to suppress the signal from fat (12-13). However, CHESS and STIR are sensitive to B_0 and B_1 field inhomogeneity, and/or reduce SNR. Dixon technique is generally less sensitive to field-inhomogeneity and it can maintain the image SNR (29). However, Dixon techniques could not be used to separate silicone implant signals (4.0 ppm chemical-shift) from fat signals (3.5 ppm chemical-shift), as they are close.

When we try to suppress one of spectrally overlapped signals, suppressing another signal is frequently beneficial to detect and characterize lesions in many clinical MR applications. For example, in the contrast-enhanced MR mammography

for patients with silicone breast implants, it is desirable to suppress both fat and implanted silicone signals to capture lesion enhancement patterns in the water signals (30). However, the number of suppressible signals using Dixon techniques is largely restricted to only one, because the output of Dixon technique is only two signals: water-dominant and fat-dominant signals. Previously, suppressing multiple signals has been achieved by combining Dixon techniques with one of other signal-suppression techniques like chemical-shift selective saturation (CHESS) and spectral short TI inversion recovery (STIR). However, incorporating with CHESS renders the process sensitive to both static (B_0) and RF (B_1) magnetic field-inhomogeneity, potentially resulting in suppressing wrong signals other than target signals to suppress. Then, it can be especially problematic for large FOV and off-isocenter imaging. On the other hand, combining with STIR can reduce the dynamic range of residual signals, while waiting for signal null-time of a target signals to suppress (29).

In this chapter, a novel generalized chemical-shift imaging technique was developed to include both T_1-contrast and chemical-shift for signal separation, aiming to overcome aforementioned limitations of Dixon techniques. The primary motivation for this work is that, although two signals may overlap in the chemical-shift domain, they may exhibit different T_1 relaxation-times. In this event, inversion RF pulses can introduce additional phase difference between the spectrally overlapped signals in order to make them differentiable in the image phase domain. Moreover, we will show that the proposed technique can perform multiple signal suppressions, assuming that one of three signals is spatially isolated with other two signals. A phantom experiment

carried out on a 1.5 T clinical scanner demonstrated the generalized chemical-shift imaging technique could achieve clear and uniform ternary signal decomposition for water, fat, and silicone signals.

IV.1 Methods

In chemical-shift dependent Dixon techniques, a complex image signal can be modeled as the summation of spectral components as follows,

$$I(x,y) = \sum_{n=1}^{N} S_n(x,y) e^{j2\pi\Delta f_n(x,y)\Delta T_{shift}} e^{j\theta(x,y)} \qquad [4.1]$$

where S_n is a spectral component corresponding to the precessional frequency-shift Δf_n, ΔT_{shift} is the echo-shift from the in-phase echo-time, and $\theta(x, y)$ is the ubiquitous spatially-varying phase error due to the off-resonance frequency-shift induced by B_0 inhomogeneity, varying susceptibilities of different tissues, eddy currents, and/or complex coil sensitivity. As previously mentioned, Dixon techniques cannot decompose spectrally overlapped signals, and the spectral components are largely limited to water and fat in practice (i.e. N = 2).

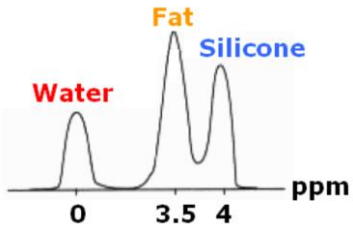

Fig 4.1 Water, fat and silicone signals in the chemical-shift domain. Fat and silicone signals overlap due to direct saturation effect and indirect saturation caused by magnetization transfer effects.

For MR mammography applications, we assume that we have three spectral components (N = 3), which are water (W with 0 ppm, T_1 = 1,000 ms, and $T_{Signal\text{-}Null}$ = 693 ms), fat (F with 3.5 ppm, T_1 = 250 ms, and $T_{Signal\text{-}Null}$ = 173 ms), and silicone (S with 4.0 ppm, T_1 = 950 ms, and $T_{Signal\text{-}Null}$ = 658 ms) signals (17). In this example, spectrums of fat and silicone signals are close and partially overlapped in the chemical-shift domain, as illustrated in Figure 4.1. To extend the ability of the Dixon technique to separate spectrally indistinguishable components with distinct T_1 times, a generalized chemical-shift imaging pulse sequence incorporating both T_1-contrast and chemical-shift was developed, as illustrated in Figure 4.2. The pulse sequence is basically an inversion-recovery pulse sequence with the echo-time shifted by ΔT_{shift}. By carefully selecting inversion-time (TI) between two signal null-times of S and F, we can create an opposing (180°) phase difference (where S maps to negative intensity and F maps to positive intensity), as illustrated in Figure 4.3.

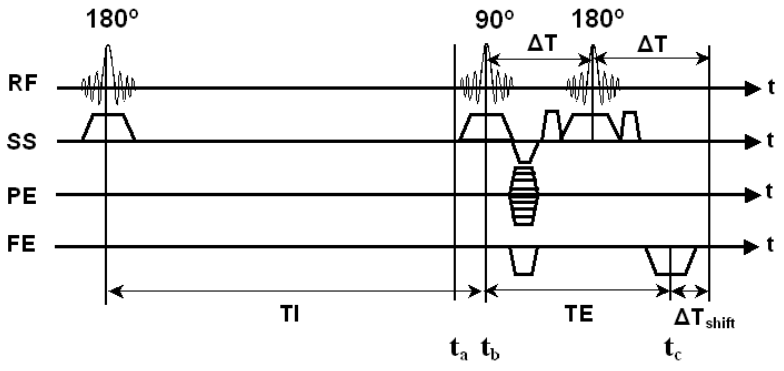

Fig 4.2 The pulse sequence diagram of the generalized chemical-shift imaging technique using both T_1-contrast and chemical-shift. In addition to the echo-shift, a 180º inversion pulse is inserted.

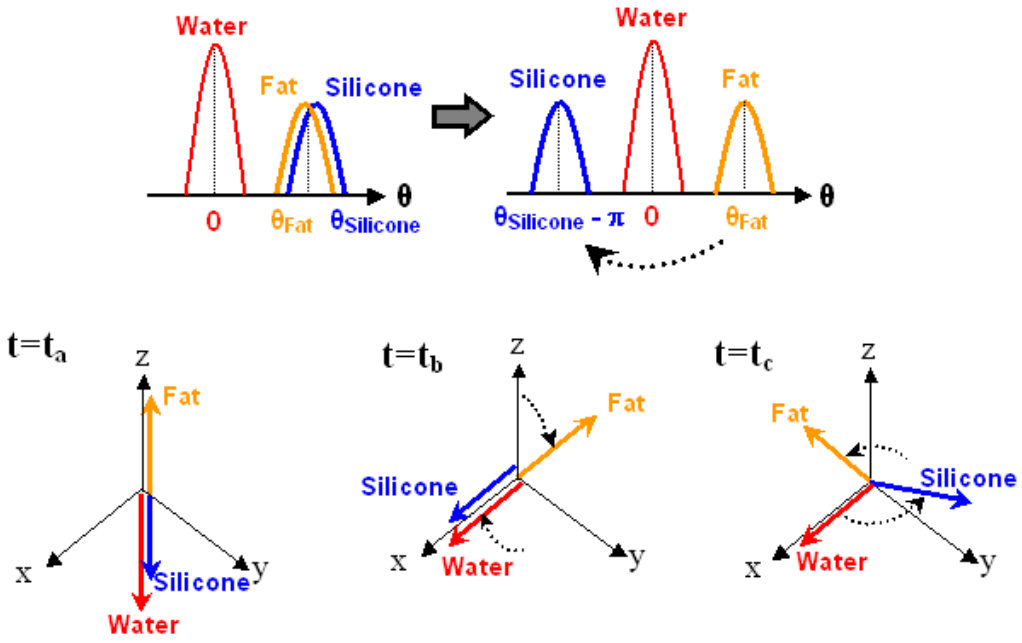

Fig 4.3 The effect of a RF inversion pulse on the image phase. The inversion pulse in Fig 4.2 can introduce the 180° phase difference between fat and silicone signals by carefully selecting TI to between two signal-null times of them. The evolution of magnetizations in the rotating reference frame. (t_a) before 90º RF pulse; (t_b) after 90º RF pulse; and (t_c) at shifted echo-time (See Fig 4.2).

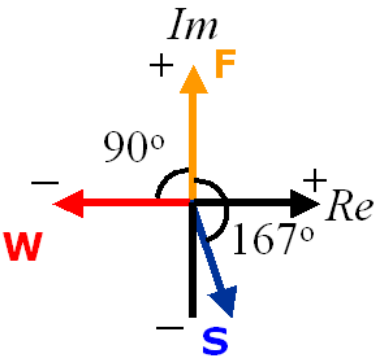

Fig 4.4 The relative signal displacement of water (W), fat (F) and silicone (S) signals acquired using the proposed pulse sequence. The, phase difference between F and S signals is 167°. On the other hand, the phase difference between W and F signals is orthogonal (90°).

Afterwards, a spin-echo pulse sequence with echo-time shifted by ΔT_{shift} is invoked at t_b to produce orthogonal (90°) phase difference between W and F at t_c. The relative signal displacement of three signals acquired using the developed pulse sequence is shown in Figure 4.4. Then, the acquired image can be modeled as,

$$I(x,y) = (-W(x,y) + jF(x,y) + e^{-j77^{o}}S(x,y))e^{j\theta(x,y)} \quad [4.2]$$

where $\theta(x,y)$ is the spatially varying background phase error.

The image phase, $\theta(x,y)$, can be estimated in many methods. In this dissertation, we extend the phase correction method introduced in chapter III to a ternary adaptive Markov random field model in order to process phase correction for three chemical species. A posteriori probability, $P(\theta|\Phi)$, is maximized by minimizing a potential function depending on where region-growing is initialized,

Case I) initial seed: water-dominant:

$$\text{If } V(\Theta) < V(\Theta + \frac{1}{2}\pi) \text{ and } V(\Theta - \frac{103}{180}\pi), \text{ then intrinsic phase} = -\pi \quad [4.3]$$

$$\text{If } V(\Theta + \frac{1}{2}\pi) < V(\Theta) \text{ and } V(\Theta - \frac{103}{180}\pi), \text{ then intrinsic phase} = \frac{1}{2}\pi \quad [4.4]$$

$$\text{If } V(\Theta - \frac{103}{180}\pi) < V(\Theta) \text{ and } V(\Theta + \frac{1}{2}\pi), \text{ then intrinsic phase} = -\frac{77}{180}\pi \quad [4.5]$$

Case II) initial seed: fat-dominant:

$$\text{If } V(\Theta) < V(\Theta - \frac{1}{2}\pi) \text{ and } V(\Theta + \frac{167}{180}\pi), \text{ then intrinsic phase} = \frac{1}{2}\pi \quad [4.6]$$

$$\text{If } V(\Theta - \frac{1}{2}\pi) < V(\Theta) \text{ and } V(\Theta + \frac{167}{180}\pi), \text{ then intrinsic phase} = -\pi \quad [4.7]$$

$$\text{If } V(\Theta + \frac{167}{180}\pi) < V(\Theta) \text{ and } V(\Theta - \frac{1}{2}\pi), \text{ then intrinsic phase} = -\frac{77}{180}\pi \quad [4.8]$$

Case III) initial seed: silicone-dominant:

$$\text{If } V(\Theta) < V(\Theta + \frac{103}{180}\pi) \text{ and } V(\Theta - \frac{167}{180}\pi), \text{ then intrinsic phase} = -\frac{77}{180}\pi \quad [4.9]$$

$$\text{If } V(\Theta - \frac{167}{180}\pi) < V(\Theta) \text{ and } V(\Theta + \frac{103}{180}\pi), \text{ then intrinsic phase} = \frac{1}{2}\pi \quad [4.10]$$

$$\text{If } V(\Theta + \frac{103}{180}\pi) < V(\Theta) \text{ and } V(\Theta - \frac{167}{180}\pi), \text{ then intrinsic phase} = -\pi \quad [4.11]$$

Figure 4.5 illustrates the change of relative signal displacement after phase correction. Once the spatially varying phase error term ($-e^{j\theta(x,y)}$ in this example) is determined, a phase-corrected Dixon signal can be computed as follows,

$$I'(x,y) = \frac{I'(x,y)}{-e^{j\theta(x,y)}} = W(x,y) - jF(x,y) - e^{-77^{\circ}}S(x,y) \quad [4.12]$$

Then, the positive and negative parts of real and imaginary signals in the phase-corrected Dixon image are as follows,

$$Re^{+}\{I'(x,y)\} = W(x,y) \quad [4.13]$$

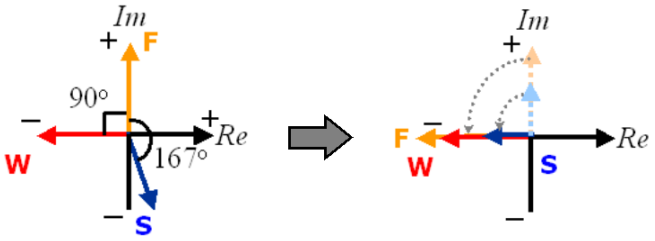

Fig 4.5 Illustration of phase correction using a ternary adaptive Markov random field model. We assume region-growing was initialized from a water-dominant pixel in this illustration.

$$\mathrm{Re}^{-}\{I'(x,y)\} = -S\cos(77^{o}) \quad [4.14]$$

$$\mathrm{Im}^{+}\{I'(x,y)\} = S\sin(77^{o}) \quad [4.15]$$

$$\mathrm{Im}^{-}\{I'(x,y)\} = -F(x,y) \quad [4.16]$$

Assuming that silicone signals are spatially isolated with both water and fat signals, Fat-only (F), water-only (W), and silicone-only signals (S) can be arithmetically decomposed as follows,

$$W(x,y) = \mathrm{Re}^{+}\{I'(x,y)\} \quad [4.17]$$

$$F(x,y) = -\mathrm{Im}^{-}\{I'(x,y)\} \quad [4.18]$$

$$S(x,y) = \sqrt{(\mathrm{Re}^{-}\{I'(x,y)\})^{2} + (\mathrm{Im}^{+}\{I'(x,y)\})^{2}} \quad [4.19]$$

Note that this technique is not limited to separate only silicone signals spectrally overlapped with fat signals, but it can be adaptively modified for other applications.

IV.2 Experiments

To demonstrate the feasibility of the proposed methodology, a phantom was constructed using a cylindrical water/fat phantom and a silicone breast implant (as shown in Figure 4.6). The water and fat phantom was constructed using a plastic water bottle, of which diameter and height are 8 cm and 20 cm, respectively. The bottle was filled with distilled water and vegetable oil half-and-half.

The proposed pulse sequence was implemented by modifying the spin-echo pulse sequence (GE Healthcare Technologies, Milwaukee, WI) and by shifting data acquisition window (ΔT_{shift}), as shown in Figure 4.2. A single channel head coil was

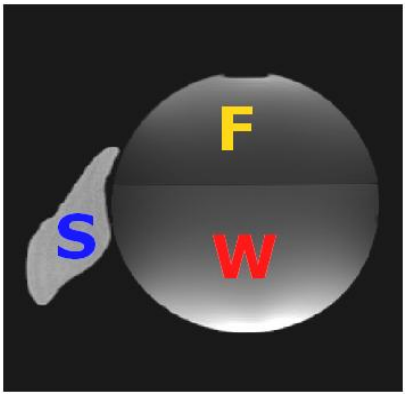

Fig 4.6 A phantom constructed using distilled water (W), vegetable oil (F) and a silicone breast implant (S).

used for imaging on a 1.5-Tesla Excite scanner with scan parameters: TR / TE = 4 sec / 30 ms, TI = 300 ms, data matrix = 256 × 256, RBW (Receiver Bandwidth) = 16 kHz, and FOV = 25 cm × 25 cm. The ΔT_{shift} was set to 1.15 ms, which is corresponding to 90º phase difference between water/fat signals at 1.5 T.

For comparison, a conventional single-point Dixon image (43) was acquired (without inversion pulses) using ΔT_{shift} = 1.15 ms for the 90° orthogonal phase difference between water and fat signals. All the other acquisition parameters were kept the same. This reference is to show the conventional single-point Dixon technique cannot identify silicone from fat signals, which have overlapped resonance frequency bands. In addition, three reference images were acquired to separate water, fat and silicone images. To do so, multiple signal suppressions were performed using the combination of CHESS (10-11) and STIR sequences (12-13). The CHESS technique was used to suppress water signals (0 ppm), and STIR was used to remove either fat (TI = 173 ms. at 1.5 T) or silicone (TI = 658 ms at 1.5 T) signals, respectively.

The image reconstruction codes for the proposed method were implemented in Matlab (MathWorks, Natick, MA). The reconstruction program was fully automated without requiring any user-intervention during the process. For comparison, the single-point Dixon reconstruction technique (43) was also implemented in Matlab as discussed in Section II.4.2. Separated images using both methods were visualized and compared with the separate water, fat, and silicone images obtained using CHESS/STIR.

IV.3 Results

Figure 4.7 (a) shows a 256 × 256 magnitude image acquired using the generalized chemical-shift imaging pulse sequence. The phase image is shown in Figure 4.7 (b). As illustrated, image phase of water (W), fat (F), and silicone (S) signals is all discontinuous, as phase differences between W and F signals and between F and S signals are modulated to have 90° and 167° phase difference, respectively. Figure 4.7 (c) depicts the phase error map estimated using the ternary adaptive Markov random field model used for phase correction.

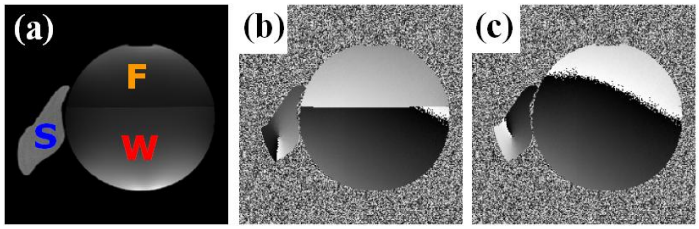

Fig 4.7 Water/fat/silicone phantom images before and after phase correction. (a) magnitude image of the phantom, (b) phase image before phase correction, and (c) estimated phase error map after phase correction.

Figure 4.8 (a-c) shows the decomposed water-only, silicone-only, and fat-only images using the proposed method, respectively. For comparison, the water-only and fat plus silicone images generated using the conventional single-point Dixon technique (43) are shown in Figure 4.8 (d) and (e). The 90º phase correction required for the single-point Dixon technique was achieved using an auto-calibrating phase correction algorithm based on the adaptive Markov random field model, which was introduced in Chapter III. As seen in Figure 4.8 (e), the conventional single-point Dixon technique cannot decompose silicone and fat signals due to the overlapping spectral signatures, thereby producing a single image containing both signals.

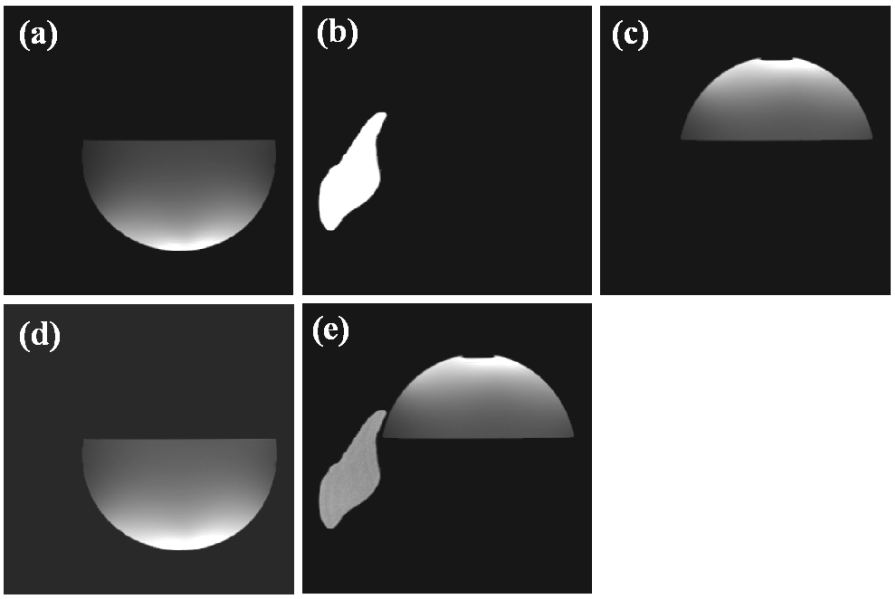

Fig 4.8 Separated images using the proposed technique (top) and the conventional single-point Dixon technique (bottom). (a) water-only (0 ppm, T_1 = 1,000 ms), (b) silicone-only (4.0 ppm, T_1 = 950 ms), (c) fat-only (3.5 ppm, T_1 = 250 ms), (d) water-only, and (e) fat and silicone images.

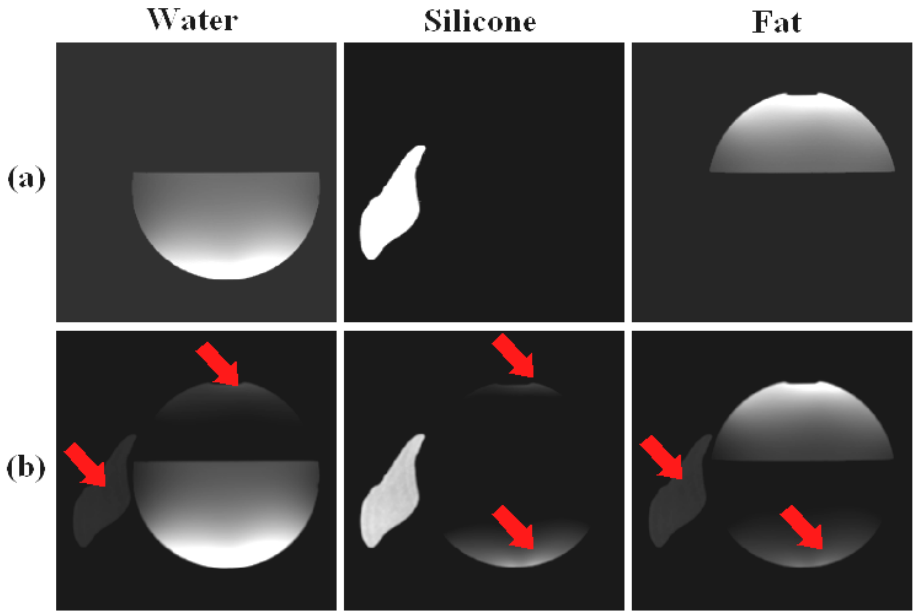

Fig 4.9 Water-only, fat-only, and silicone-only images. (a) the proposed technique, and (b) the combination of CHESS and STIR. Incomplete suppressions are indicated using arrows.

In Figure 4.9, decomposed water, fat, and silicone images using the proposed technique (in Figure 4.9 (a)) were compared with the conventional multiple signal suppression technique using the combination of CHESS and STIR (in Figure 4.9 (b)). Because selective saturation using CHESS failed due to field-inhomogeneity, signal suppressions were incomplete, as indicated using arrows in Figure 4.9 (b). Moreover, STIR reduces the SNR of decomposed signals. In contrast, the proposed technique can achieve uniform and clear signal separations, as shown in Figure 4.9 (a).

IV.4 Discussion

In this chapter, we developed a novel generalized chemical-shift imaging technique including both T_1-contrast and chemical-shift for two aims: (1) decomposing two

signals having overlapped resonance frequency bands, and (2) achieving multiple signal suppressions, assuming that one of three signals is spatially isolated with other two signals. A phantom experiment carried out on a 1.5 T clinical scanner demonstrated that the generalized chemical-shift imaging technique could achieve clear and uniform ternary signal decomposition for water, fat, and silicone signals.

The developed technique is expected to be useful for MR mammography to examine ruptures or leaks in silicone breast implants by suppressing both water and fat signals. Another clinical application is the contrast-enhanced MR mammography for patients with breast implants. Both fat and implanted silicone signal suppressions can improve tissue contrast to make it more feasible to capture lesion enhancement patterns in water signals. In practice, there are various MR clinical applications, which have two spectral overlapped components. In these applications, suppression of one signal between them frequently improves observation for the other signal providing clinically important information. The proposed technique is expected to extend the current clinical applications of Dixon water/fat imaging techniques to include separation of spectrally overlapping signal components. For example, saline is another widely used breast implant. However, Dixon techniques could not be used to examine ruptures and leaking in the implanted saline because the resonance frequencies of saline and water signals are exactly the same (but they have different T_1 times). For future work, we plan to adaptively modify the proposed technique for the saline breast implant applications. We also plan to investigate the sensitivity of the method to detect small amount of leak.

One technical limitation of the proposed method is that the spectrally overlapped (but T_1 separable) signal either with water or fat must be spatially isolated with both water and fat signals in order to make three signals separable using a single data acquisition. This may limit the practical usefulness of the proposed technique in certain applications. Nevertheless, the above assumption is still valid in many applications like silicone implant imaging.

CHAPTER V

CONTRAST-ENHANCED DIXON TECHNIQUE

In T_1-weighted MR ontological imaging, it is important to achieve large image-contrast between before and after paramagnetic contrast-agent injection to capture lesion enhancement patterns. In these MR applications, PSIR and Dixon techniques have been widely used to improve tissue contrast, the former by extending the dynamic range of image intensity (1-2) and the later by suppressing unnecessary fat signals (3-6). However, strong fat signals in PSIR imaging may hide clinically important information on water signals. In the case of Dixon techniques, signal intensity levels in the decomposed water signals are limited in the positive range.

In this chapter, we developed a contrast-enhanced Dixon technique, which can improve image-contrast using both water/fat separation and dynamic-range extension to positive/negative signal intensity levels, simultaneously. To achieve this goal, a single-point Dixon technique was incorporated with PSIR to produce 180º phase difference between contrast-enhanced positive/negative water signals, and 90º phase difference between water/fat signals, respectively. After phase correction using the adaptive Markov random field model introduced in Chapter III, contrast-enhanced water-only and fat-only images are clearly decomposed from the real and imaginary parts of phase-corrected signals for each.

To demonstrate the feasibility of the proposed methodology, a phantom was constructed using vegetable oil fat and distilled water with/without 1g/L $CuSO_4$ to

make T_1-contrast. The result of a phantom experiment performed on 4.7 T scanner shows clearly decomposed and contrast-enhanced water and fat images could be obtained. The proposed technique is expected to be useful to improve the observation for diagnostic processes such as dynamic contrast enhancement agent uptake in MR ontological imaging.

V.1 Methods

V.1.1 Contrast-Enhanced Dixon Pulse Sequence

This technique is based on the same pulse sequence, introduced in Figure 4.2 of Chapter IV, which can be considered as the combination of PSIR with a single-point Dixon technique where there is an orthogonal (90°) phase difference between water and fat signals. By carefully selecting an inversion-time (TI), we can enhance the contrast of two water signals, as illustrated in Figure 5.1. Following the inversion pulse, a spin-echo pulse sequence with the shifted echo-time by ΔT_{shift} can be used to produce

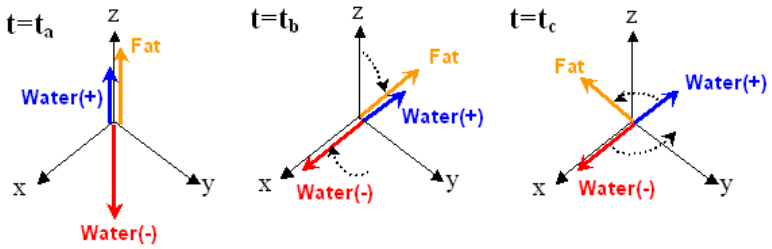

Fig 5.1 Evolution of magnetizations in the rotating reference frame. (t_a) before 90º RF pulse; (t_b) after 90º RF pulse; and (t_c) at shifted echo-time. The inversion pulse in Fig 4.2 can extend the dynamic range of two water signals to be in [$-M_0$, $-M_0$]. Then, shifted echo-time is used to produce orthogonal (90°) phase difference between water and fat signals at $t = t_c$ (t_a, t_b, and t_c are defined in Fig 4.2).

orthogonal (90°) phase difference between contrast-enhanced water and fat signals at t_c. Then, the acquired image can be modeled as,

$$I(x,y) = (W(x,y) + F)e^{j\theta(x,y)} \quad [5.1]$$

where $\theta(x,y)$ is the spatially varying background phase error, F is all positive fat-signals, W is contrast-enhanced water signals such that $-M_o \le W \le M_o$, where M_o is the longitudinal equilibrium magnetization of water spins.

In order to estimate $\theta(x,y)$, we extend the phase correction method introduced in Section III.1.1 to a ternary adaptive Markov random field model, as discussed in Section III.1.3. A posteriori probability, $P(\theta|\Phi)$, is maximized by minimizing a potential function depending on where region-growing is initialized,

Case I) initial seed: positive water-dominant:

$$\text{If } V(\Theta) < V(\Theta - \tfrac{1}{2}\pi) \text{ and } V(\Theta - \pi), \text{ then intrinsic phase} = 0 \quad [5.2]$$

$$\text{If } V(\Theta - \tfrac{1}{2}\pi) < V(\Theta) \text{ and } V(\Theta - \pi), \text{ then intrinsic phase} = \tfrac{1}{2}\pi \quad [5.3]$$

$$\text{If } V(\Theta - \pi) < V(\Theta) \text{ and } V(\Theta - \tfrac{1}{2}\pi), \text{ then intrinsic phase} = -\pi \quad [5.4]$$

Case II) initial seed: negative water-dominant:

$$\text{If } V(\Theta) < V(\Theta + \tfrac{1}{2}\pi) \text{ and } V(\Theta + \pi), \text{ then intrinsic phase} = -\pi \quad [5.5]$$

$$\text{If } V(\Theta + \tfrac{1}{2}\pi) < V(\Theta) \text{ and } V(\Theta + \pi), \text{ then intrinsic phase} = \tfrac{1}{2}\pi \quad [5.6]$$

$$\text{If } V(\Theta + \pi) < V(\Theta) \text{ and } V(\Theta + \tfrac{1}{2}\pi), \text{ then intrinsic phase} = 0 \quad [5.7]$$

Case III) initial seed: fat-dominant:

$$\text{If } V(\Theta) < V(\Theta - \frac{1}{2}\pi) \text{ and } V(\Theta + \frac{1}{2}\pi), \text{ then intrinsic phase} = \frac{1}{2}\pi \qquad [5.8]$$

$$\text{If } V(\Theta - \frac{1}{2}\pi) < V(\Theta) \text{ and } V(\Theta + \frac{1}{2}\pi), \text{ then intrinsic phase} = -\pi \qquad [5.9]$$

$$\text{If } V(\Theta + \frac{1}{2}\pi) < V(\Theta) \text{ and } V(\Theta - \frac{1}{2}\pi), \text{ then intrinsic phase} = 0 \qquad [5.10]$$

Figure 5.2 illustrates the process of phase correction using the ternary adaptive Markov random field model, assuming that region-growing is initialized from a positive water-dominant pixel. Once the spatially varying phase error term ($e^{j\theta(x,y)}$) is determined, phase-corrected signals can be acquired as such,

$$I'(x,y) = \frac{I'(x,y)}{e^{j\theta(x,y)}} = W(x,y) + jF(x,y) \qquad [5.11]$$

Then, the contrast-enhanced water and fat signals can be decomposed simply by,

$$W(x,y) = \mathrm{Re}\{I'(x,y)\} \qquad [5.12]$$

$$F(x,y) = \mathrm{Im}\{I'(x,y)\} \qquad [5.13]$$

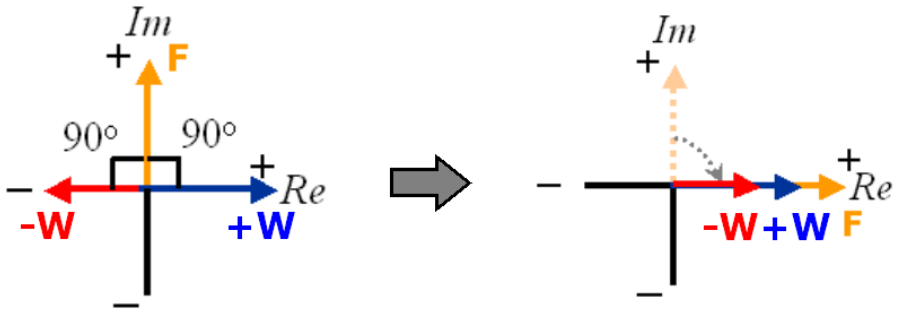

Fig 5.2 Illustration of phase correction using the adaptive Markov random field model.

V.1.2 Contrast Evaluation

To evaluate image-contrast enhancement using the proposed technique, two ROIs are selected in the decomposed water-only image. Image-contrast can be calculated by measuring mean image-intensity difference between two ROIs defined as,

$$\text{Contrast} = \frac{1}{N_{ROI_{Water+}}} \sum_{(x,y) \in ROI_{Water+}} I(x,y) - \frac{1}{N_{ROI_{Water-}}} \sum_{(x,y) \in ROI_{Water-}} I(x,y) \qquad [5.14]$$

where ROI_{Water+} and ROI_{Water-} are selected ROIs in positive-contrast and negative-contrast water signal regions, respectively. Then, the calculated image-contrast was compared with that of the conventional single-point Dixon discussed in Section II.4.2, which is acquired as the reference.

V.2 Experiments

To demonstrate the feasibility of the proposed methodology, a cylindrical phantom was constructed using a plastic box (4 cm diameter and 7 cm height). As shown in Figure 5.3, three compartments of the phantom were filled with: (1) vegetable oil fat (3.5 ppm, T_1 = 250 ms at 4.7 T), (2) distilled water (0 ppm, T_1 = 4,250 ms at 4.7 T), and (3) water doped with 1g/L $CuSO_4$ (0 ppm, T_1 = 780 ms at 4.7 T) (57). The $CuSO_4$ was added to create T_1 contrast between two aqueous signals.

The proposed pulse sequence was implemented on a 4.7 T / 33 cm Bruker scanner. Images were acquired with a single channel birdcage coil using the following scan parameters: TR = 3 s, TE = 30 ms, BW_{RF} = 1 kHz, ST = 3 mm, FOV = 10 cm, and data matrix = 256 × 256. The acquisition window was shifted by ΔT_{shift} = 357 us from

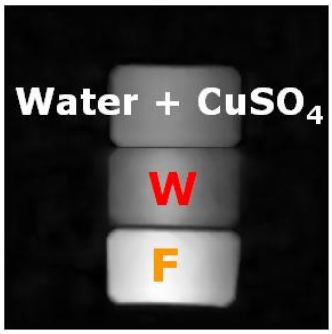

Fig 5.3 A phantom constructed using water doped with 1g/L $CuSO_4$, distilled water (W), and vegetable oil (F).

the in-phase echo-time to create orthogonal 90° phase difference between water and fat signals at 4.7 T (3.5 ppm chemical-shift water/fat). Inversion time (TI) was set to 800 ms, which is between two signal-null times of distilled water and water doped with 1g/L $CuSO_4$ signals, which are designed to be negative and positive contrast water signals in the reconstructed image. For the reference, a single-point Dixon images was acquired using ΔT_{shift} = 357 us for 90° orthogonal phase difference between water and fat signals without the inversion pulse. All other acquisition parameters were kept the same.

Processing algorithms for the proposed method were implemented in Matlab (MathWorks, Natick, MA). The reconstruction program was fully automated without requiring any user-intervention during the process. For comparison, the single-point Dixon algorithm was also implemented in Matlab, as introduced in Section II.4.2. Separated images using both methods were visualized and compared.

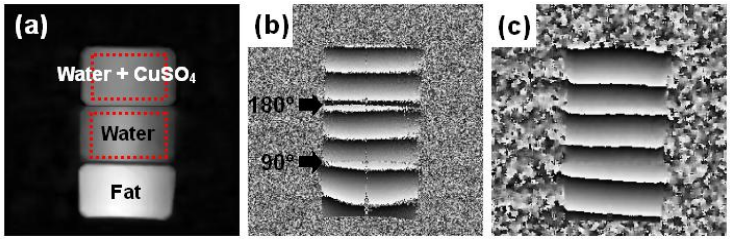

Fig 5.4 Water/fat phantom magnitude and phase images (before and after phase correction). (a) magnitude image of the phantom, (b) phase image before phase correction. Note 90º or 180º phase difference at boundaries, and (c) estimated phase error map after phase correction using a ternary adaptive Markov random field model.

V.3 Results

Figure 5.4 (a) shows a 256 × 256 magnitude image acquired using the contrast-enhanced Dixon pulse sequence. The two water compartments show similar image intensity levels. The phase image is shown in Figure 5.4 (b). As illustrated, the polarity difference of two water compartments is reflected in the phase discontinuity.

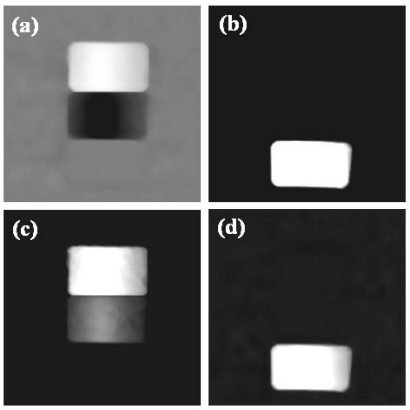

Fig 5.5 The separated images using the contrast-enhanced Dixon and the conventional single-point Dixon techniques. (a) contrast-enhanced water-only, and (b) contrast-enhanced fat-only images by the proposed technique, and (c) water-only, and (d) fat-only images by the conventional one-point Dixon technique.

Table 5.1 Contrast comparison between the proposed technique and the conventional single-point Dixon technique. In this experiment, the proposed technique could improve image-contrast between two water compartments by 1.6 times compared with the conventional Dixon technique.

	Contrast-Enhanced Dixon	One-Point Dixon
Mean Signal Intensity at ROI_{+W}	4.35	4.32
Mean Signal Intensity at ROI_{-W}	-0.90	1.08
Contrast	5.25	3.24
Contrast Improvement	1.6 times	

Also, note the orthogonal (90º) phase difference between fat and water signals. Figure 5.4 (c) shows the estimated phase error map after phase correction using a ternary adaptive Markov random field model.

In Figure 5.5, the decomposed water-only and fat-only images using the proposed technique (a-b) were compared with decomposed images by the conventional single-point Dixon technique (c-d). The signal intensity levels were adjusted to the same for comparison. The contrast-enhancement of the proposed technique over the conventional single-point Dixon technique was evaluated using Eq. [5.14], and the result was summarized in Table 5.1. The ROIs selected for positive-contrast and negative-contrast water signal regions are illustrated in Figure 5.4 (a). The proposed technique could achieve the 1.6 times higher image-contrast, compared with the conventional single-point Dixon technique.

V.4 Discussion

In this chapter, we developed a contrast-enhanced Dixon technique to extend the limited dynamic range of decomposed water signals to both positive/negative image intensity levels, so that tissue contrast can be improved. A phantom study performed on a 4.7 T Bruker Scanner demonstrated the feasibility of the proposed methodology, successfully decomposing contrast-enhanced water and fat signals. The proposed technique could achieve the 1.6 times higher image-contrast, compared with the conventional single-point Dixon technique.

For MR contrast-agent enhanced oncological imaging applications, the proposed technique is expected to be useful to improve the capability of capturing lesion enhancement patterns between before and after contrast-agent injection by suppressing strong fat signals, as well as by extending the dynamic range of decomposed water-only signals to both positive/negative signal intensity levels.

The inversion RF pulses inserted to increase image-contrast of water signals increase total scan time. In the next chapter, we will discuss parallel imaging methods (39-42, 58-61) for Dixon phase-sensitive imaging to improve scan efficiency, and tissue contrast simultaneously.

CHAPTER VI

CONTRAST-ENHANCED SINGLE-ECHO ACQUISITION IMAGING

One limitation of currently used phase-sensitive Dixon contrast-enhancing techniques is long scan-time due to two major reasons: (1) long scan-time to acquire multiple phase-encoding data for Dixon imaging itself, and (2) additional calibration scans for phase correction, which are required for Dixon water and fat decomposition. They have limited the spatio-temporal resolution of phase-sensitive MR imaging methods.

In this chapter, we developed an ultra-fast and auto-calibrating contrast-enhanced SEA imaging technique, which can acquire water-only and fat-only images within TR and without requiring any time-consuming calibration scan. To improve scan-efficiency, a single-point Dixon method (43) was incorporated with a fully parallel single-echo acquisition (SEA) imaging technique (39-42). In SEA imaging, simultaneously acquired 64 echoes are combined to form a 2-D image. However, image lines from 64 SEA channels have different phase error levels. To overcome this issue, we developed an auto-calibrating 1-D phase correction algorithm to decompose water and fat signals independently for each image line. The algorithm assumes smoothness of the phase field, but it does not require any additional reference scan. After phase correction, line-by-line separated water and fat image lines were combined using image correlations, assuming that there is not signal-void between adjacent channel signals.

The proposed technique was implemented on a 64-channel SEA imaging system and tested using a phantom study. The result of an experiment demonstrated that 2-D water-only and fat-only images could be acquired using a single echo. Image-contrast between two water signals was improved about 2.4 times, compared with the conventional SEA imaging technique.

Although, the penetration depth of a massive SEA phased coil array is limited due to the small size of the coil element in one direction (39-42), the truly high frame-rate of SEA appeals to several potential applications in animal imaging. Animal studies using conventional MRI are prone to get ghosting artifacts coming from very fast peristaltic movement of internal organs and/or breathing motion of animals (62). For MR animal studies using small lab animals, which are still available for the limited penetration depth beyond a few centimeters, the proposed technique is expected to be useful to improve image-contrast by fat-suppression and to provide more accurate dynamic information.

VI.1 Methods

VI.1.1 Single-Point Dixon SEA Pulse Sequence

A single-point Dixon pulse sequence (43) was used in this proposed technique. It is essentially a spin-echo sequence with a shifted read-out data acquisition window. The echo shift produces relative phase difference between water and fat signals that will be used later to separate water and fat components. In multi-point Dixon techniques (3-6), because two or more equations (one from the real part and the other from the

imaginary part of the image) are needed to decompose water and fat signals, 0° (i.e. in-phase) and 180° (i.e. out-of-phase) phase difference will result in a degenerate case. In our experiment, ΔT_{shift} is carefully designed so that phase difference between water and fat signals will be 90° (i.e. orthogonal). The echo acquired is frequency-encoded using a linear gradient. Because the spatial localization along the phase-encoding direction is completely accomplished by localized coil sensitivity, only one echo from each channel is acquired (39-42). The echo is acquired with a certain phase-encoding gradient to compensate for the phase ramp due to the inherent wavelength effect of small coil size, as described in (41). The single echo from each of the 64 channels will be individually 1-D Fourier transformed, stacked, and processed to form the desirable water/fat images.

Using the pulse sequence as described above, the frequency encoded echo signal from the *c*-th channel can be expressed as,

$$D_C(k_x) = \iint [W(x,y)+e^{j\varphi}F(x,y)]\left|S_c(x,y)\right| e^{j\theta_c(x,y)} e^{-jk_x x} dxdy \qquad [6.1]$$

where k_x is the spatial frequency induced by the frequency encoding gradient, W(x, y) and F(x,y) are water and fat signals, φ is the chemical-shift induced phase by the shifted echo-time, $S_c(x,y)$ is coil sensitivity, and $\theta_c(x,y)$ is the non-chemical shift phase error introduced by various possible sources such as B_0 field inhomogeneity, varying susceptibilities of different tissues, eddy currents, and complex coil sensitivity. In this work, φ is set to be 90° so that, after the non-chemical shift phase error is estimated and removed, water/fat can be easily decomposed as the real and imaginary parts of the complex pixels in the reconstructed image.

In SEA imaging, it assumes that the coil-sensitivity is very localized along the y-direction, for example to the order of the pixel size. Thus, the above equation can be reduced to

$$D_c(k_x) \approx \int [W(x,y_c) + e^{j\varphi}F(x,y_c)]\left|S_c(x,y_c)\right| e^{j\theta_c(x,y_c)} e^{-jk_x x} dx \qquad [6.2]$$

where y_c is the central location of the c-th coil along y-direction. After 1-D inverse Fourier transform of $D_c(k_x)$, an image line can be formed as,

$$\hat{I}_c(x) \approx [\hat{W}_c(x) + e^{j\varphi}\hat{F}_c(x)]e^{j\theta_c(x)} \qquad [6.3]$$

where $\hat{W}_c(x) = W(x,y_c)\cdot\left|S_c(x,y_c)\right|$ and $\hat{F}_c(x) = F(x,y_c)\cdot\left|S_c(x,y_c)\right|$, i.e., sensitivity-weighted water and fat signals, respectively. Then, a complex 2-D SEA image can be reconstructed by stacking all 64 image lines $\hat{I}_c(x)$, c = 1,2,…,64, together. In the absence of the coil-dependent phase error, $\theta_c(x)$, water and fat signals can be resolved straightforwardly by matching the real and imaginary parts on both sides of the above equation,

$$\mathrm{Re}\{\hat{I}_c(x)\} \approx \hat{W}_c(x) + \hat{F}_c(x)\cos\varphi \qquad [6.4]$$

$$\mathrm{Im}\{\hat{I}_c(x)\} \approx \hat{F}_c(x)\sin\varphi \qquad [6.5]$$

In practice, $\theta_c(x)$ can vary significantly from channel to channel and from location to location, therefore it needs to be estimated and corrected in order to resolve water and fat signals. In this work, φ is set to be 90° to simplify this separation.

Currently available techniques estimate $\theta_c(x)$ depending on separately acquired low-resolution reference images. However, motions, flows, and system phase

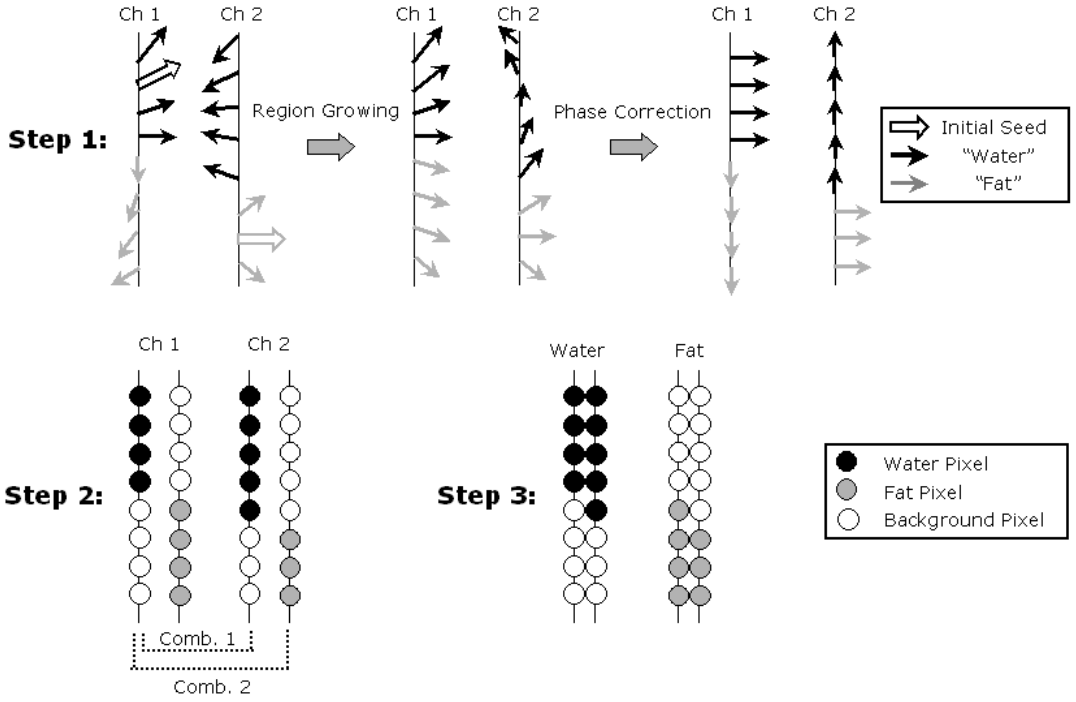

Fig 6.1 Illustration of the proposed water and fat decomposing method for SEA imaging. (Step 1) channel-by-channel phase correction by 1-D region-growing, (Step 2) intermediate water and fat decomposition, and (Step 3) channel combination based on correlation between intermediate water/fat images.

instability can lead to significant changes in this term. Multiple calibration scans may be performed periodically during the dynamic imaging to capture time-variant phase information, but doing so will impair high frame-rates of the SEA imaging. A more efficient phase correction method is to use a 2-D phase correction algorithm assuming that the image phase variation is smooth (44). However, because each channel has different phase factors, the 2-D phase map is not a smooth field and estimating it using a 2-D region-growing algorithm is difficult. To address this problem, an auto-calibrating 1-D region-growing algorithm based on the MRF model was developed. The new algorithm consists of three steps: (1) channel-by-channel phase correction; (2)

intermediate water and fat decomposition; and (3) channel combination based on correlation between intermediate water/fat image lines. These three steps are illustrated in Figure 6.1.

VI.1.2 Channel-by-Channel Phase Correction

The phase correction of each channel is performed using a 1-D region-growing algorithm. It is based on an assumption that the phase term, $\theta_c(x)$, is a spatially smooth function within the single image line from the corresponding channel. This smooth component can be differentiated from the phase change due to water/fat chemical shift. In each channel, a seed pixel is chosen from the complex SEA image line and a 1-D region-growing algorithm is applied from the initial seed. To improve the robustness, a seed is initialized from a pixel having the minimum phase difference with its neighbors. In addition, at each intermediate step during the region-growing, a phase vector is computed as the complex sum of all the phase-corrected pixels within the neighborhood. The region-growing is based on the phase continuity between this phase vector and a new pixel to be considered. Specifically, if the angular difference between a new pixel and the current phase vector is over than 45° (the half of phase difference between water/fat signals), it is determined to have a water/fat phase jump and 90° phase correction is applied to the new pixel being processed. Otherwise, the region will simply grow to the new pixel. As shown in the earlier work (44), using a neighborhood of pixels as a baseline for region-growing has several advantages over the region-growing methods based on pixel pairs. First, the noise effect on the phase vector can be minimized, as the complex vector sum of random Gaussian noise can be approximated

into zero. Secondly, the method can largely prevent the accidental phase correction errors from a noisy pixel to propagate during the region-growing process, therefore limits the error to an isolated pixel rather than the whole image region otherwise.

VI.1.3 Intermediate Water and Fat Decomposition

For each channel, the 1-D region-growing process provides an estimate of the phase error term, $\hat{\theta}_c(x)$. Assuming that region-growing algorithm starts from a water pixel, the phase-corrected image line can be calculated as,

$$I'(x) = \hat{I}(x) \times e^{-j\hat{\theta}_c(x)} \approx \hat{W}_c(x) + j\hat{F}_c(x) \qquad [6.6]$$

for $1 \le c \le 64$. Then, intermediate water and fat portions of the image line can be decomposed as follows,

$$\hat{W}_c(x) = \mathrm{Re}\{I'\} \qquad [6.7]$$

$$\hat{F}_c(x) = \mathrm{Im}\{I'\} \qquad [6.8]$$

However, if a fat-dominant pixel was chosen as the initial seed, the phase correction will introduce an additional $\pi/2$ phase term as such,

$$I'(x) = \hat{I}(x) e^{-j[\hat{\theta}(x) + \frac{\pi}{2}]} = (\hat{W}_c(x) + j\hat{F}_c(x)) e^{-j\frac{\pi}{2}} \qquad [6.9]$$

Therefore,

$$\hat{W}_c(x) = -\mathrm{Im}\{I'\} \qquad [6.10]$$

$$\hat{F}_c(x) = \mathrm{Re}\{I'\} \qquad [6.11]$$

The step 2 in the Figure 6.1 shows the effect of the seed selection in the water and fat decomposition. Note that due to the channel phase variation, the seed could be water

and fat rather randomly from channel to channel. This ambiguity will be addressed next using correlation between channel signals.

VI.1.4 Channel Combination

To form consistent 2-D water and fat images, the particular ambiguity must be solved: identifying if the selected initial pixel was water-dominant, or fat-dominant in the previous processing step. To solve this ambiguity, we use the correlation between intermediate water lines acquired in the previous step across adjacent channels. Specifically, assuming that water and fat tissues have spatial continuity from channel to channel, two water signals from adjacent channels should have stronger spatial correlation than that of a water signal and a fat signal. Similarly, water signal and fat signal from the adjacent channels should be less correlated. To effectively use this constraint, we define a parameter called sum of point-by-point multiplication index (SPMI),

$$\mathrm{SPMI}_{WW}(y_c, y_{c+1}) = \sum_{x=1}^{N_x} \left|\hat{W}_c(x,y)\right| \cdot \left|\hat{W}_{c+1}(x,y_{c+1})\right| \qquad [6.12]$$

$$\mathrm{SPMI}_{WF}(y_c, y_{c+1}) = \sum_{x=1}^{N_x} \left|\hat{W}_c(x,y_c)\right| \cdot \left|\hat{F}_{c+1}(x,y_{c+1})\right| \qquad [6.13]$$

where $\hat{W}$ and $\hat{F}$ are intermediate water and fat lines that might be mislabeled. The combination process starts by selecting an arbitrary beginning channel. Then, based on SPMI, water and fat images in the adjacent channels are determined, as illustrated in Figure 6.2. Specifically, if $\mathrm{SPMI}_{WW} < \mathrm{SPMI}_{WF}$, the water and fat image lines of the next channel are swapped. Assuming that there is no complete signal-void in any of the

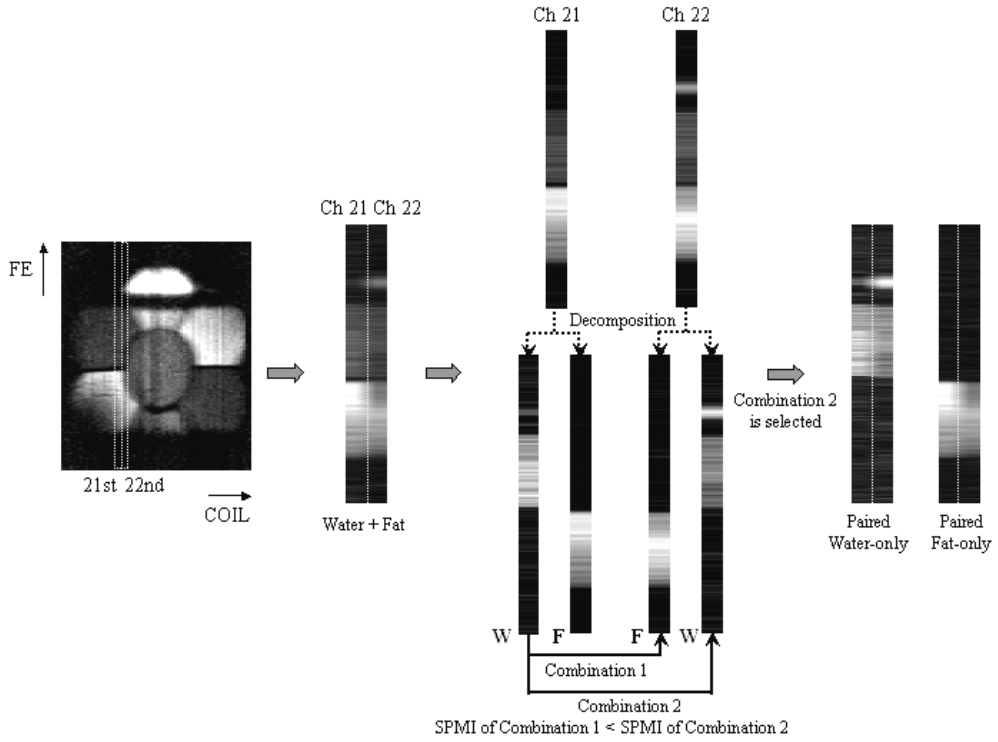

Fig 6.2 Channel combination based on correlation between intermediate water and fat images. The graph shows how the 21st and 22nd channels are combined. In the example, water/fat images defined in the 22nd channel were swapped according to a correlation factor, SPMI.

channel image lines, this process can be propagated to all channels to form consistent 2-D water and fat images.

Note that, in T_1-weighted SEA images, the fat image has higher intensity than the water image usually. This fact can be used to determine which image should be assigned as the fat-only image. Specifically, for each image, a binary mask is created using an intensity threshold, which equals to three times of the standard deviation of the noise pixels (i.e. pixels in the background). Then, an image with the higher average intensity (of all pixels in its own mask) is assigned as the fat-only image.

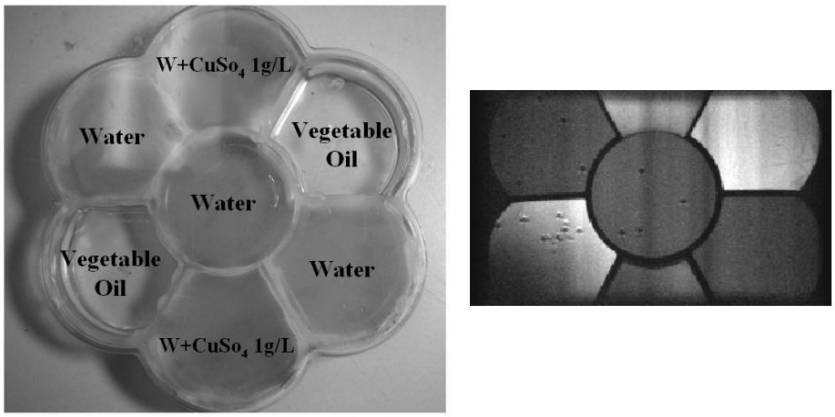

Fig 6.3 Illustration of the phantom used in the experiment. (Left) partitioned space filled with different materials like vegetable oil fat (T_1 = 250 ms), water doped with 1g/L $CuSO_4$ (T_1 = 780 ms), and distilled water (T_1 = 4,250 ms) at 4.7 T. (Right) the 256 × 256 phantom image with conventional spin-echo sequence.

VI.2 Experiments

VI.2.1 Phantom Study

To test the proposed methodology, a cylindrical phantom (as illustrated in Figure 6.3) was constructed using a 12 cm diameter plastic box with seven compartments filled with different materials: (1) vegetable oil fat (T_1 = 250 ms at 4.7 T), (2) distilled water (T_1 = 4250 ms at 4.7 T), and (3) water doped with 1g/L $CuSO_4$ (T_1 = 780 ms at 4.7 T) (57). Single-point Dixon SEA images were acquired on a 4.7 T / 33 cm Bruker Scanner with a 64-channel linear array (2 mm by 81 mm planar-pair elements using the proposed sequence). Scan parameters were: TR = 100 ms, TE = 20 ms, RBW = 50 kHz, ST = 3 mm, N_x = 256, and FOV = 14 cm. For the spin-echo sequence shown in the Figure 2.5, the acquisition window was shifted by ΔT_{shift} = 357 us from the in-phase echo time to create orthogonal 90° phase difference between water and fat signals at

4.7 T.

A 256 × 256 fully encoded in-phase image was scanned using a regular spin-echo protocol with the same scan parameters, but with 256 phase encodings steps to show the structures. Then, 256 × 256 dataset with a shifted acquisition window (with the same ΔT_{shift}) was acquired. For SEA reconstructions, the phase-encoding line with overall phase ramp compensation effect was taken from the fully encoded dataset as the single echo to be used. The proposed algorithm and water and fat combination using SPMI were implemented in Matlab (MathWorks, Natick, MA). The full procedure was fully automated.

VI.2.2 Contrast Evaluation

The conventional image-contrast evaluating method (i.e. measuring signal ratio or absolute signal difference between tissues) is not useful to evaluate contrast-enhancement by water and fat decomposition, because the absolute image intensity level does not change before and after separation. To evaluate the effective image-contrast from water/fat separation, we define a factor called normalized contrast by dynamic-image range (NCDR),

$$NCDR = \frac{\left| \frac{1}{N_{ROI_1}} \sum_{(x,y) \in ROI_1} I(x,y) - \frac{1}{N_{ROI_2}} \sum_{(x,y) \in ROI_2} I(x,y) \right|}{I_{max} - I_{min}} \qquad [6.14]$$

where I_{max} and I_{min} are the maximum and the minimum signal intensities in the whole image respectively, and N_{ROI1} and N_{ROI2} are number of pixels in two ROIs, respectively.

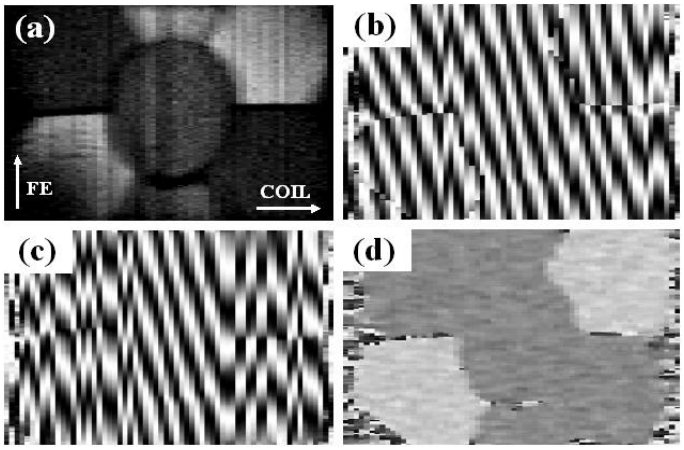

Fig 6.4 SEA image and the phase correction effects. (a) SEA magnitude image, (b) SEA phase image (shown after taken cosine). Note the channel-to-channel phase variations and the 90° phase jump between water and fat compartments, (c) the corresponding phase image after 1-D region-growing, and (d) chemical-shift induced phase image (0° and 90°) extracted after the phase correction.

VI.3 Results

Figure 6.3 (b) shows a high-resolution sum-of-squares (SOS) magnitude image from the 256 × 256 in-phase data. Only the central 12 cm × 8 cm portion of ROI is displayed in the SOS image for better visualization. Figure 6.4 (a) and (b) show the SEA magnitude and phase images (after taking the cosine value), respectively. Note the low image-contrast between water compartments due to strong fat signals in Figure 6.4 (a). Also note that, due to the channel difference, the phase image in Figure 6.4 (b) looks rather random. Figure 6.4 (c) shows the phase error-map corresponding to Figure 6.4 (b) after 1-D phase correction. Although there are partial volume effects, the algorithm was able to successfully identify the 90° intrinsic phase within each channel. But, the phase between adjacent channels is not all consistent. Figure 6.4 (d) shows the phase

map after inconsistent image phase between adjacent channels is corrected using SPMI, and the phase error is removed from the original SEA image, leaving only 0° and 90° phase values (corresponding to water and fat, respectively).

Figure 6.5 shows the effect of phase correction on image separation and image-contrast. The intermediate water/fat images after 1-D phase correction are shown in Figure 6.5 (a) and (b), respectively. The incorrectly assigned water and fat lines are due to selecting fat pixels as seeds in some channels. After correlation based channel combination, the final water/fat reconstructions are shown in Figure 6.5 (c) and (d), respectively.

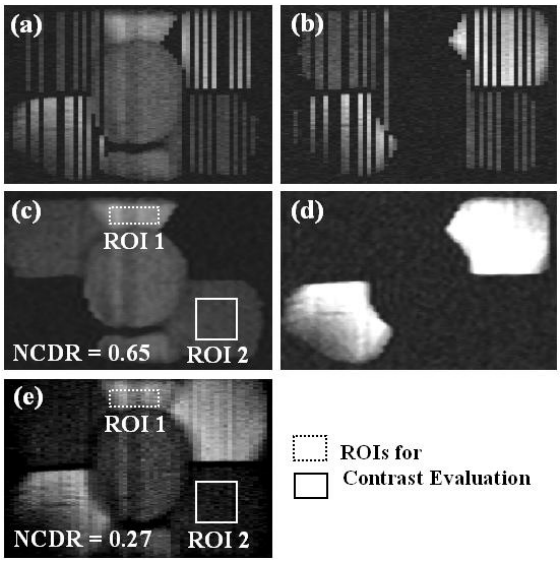

Fig 6.5 Intermediate water and fat images before and after channel combination. (a) water image, (b) fat image before channel combination, (c) water-only image and (d) fat-only image after channel combination. Stripes in (a-b) were corrected by processing channel combination. Note the significant contrast improvement in (c) as compared with (e), the conventional SEA image for a reference.

Table 6.1 Evaluation for contrast-enhancement using NCDR. In this experiment, the proposed technique could improve effective image-contrast between two water compartments by 2.4 times compared with the conventional SEA image.

	Contrast-Enhanced SEA	Conventional SEA
I_{Max}	1.82	2.95
I_{Min}	1.02	1.06
Mean Signal Intensity at ROI 1	1.79	1.76
Mean Signal Intensity at ROI 2	1.27	1.25
NCDR	0.65	0.27
NCDR Improvement	2.4 times	

Compared with water/fat images with the phantom image in Figure 6.3, it shows that the proposed algorithm correctly produces water-only and fat-only partitions. Note that, as compared with Figure 6.4 (a), the image-contrast between water compartments has been significantly enhanced due to the removal of fat signals. Contrast enhancement using the proposed method was quantitatively evaluated by measuring image-contrast between the two compartments using NCDR. Selected regions of interest are illustrated in Figure 6.5 (c) and (e). In this experiment, it was shown that water/fat separation could improve image-contrast between the water compartments by 2.4 times compared with the conventional SEA image, as summarized in Table 6.1.

To quantitatively evaluate the water/fat separation based on the proposed algorithm, ground-truth water and fat maps were manually selected from the fully-encoded 256 × 256 reference image, as illustrated in Figure 6.6 (a) and (b). Then, SEA water-only and fat-only maps (shown in Figure 6.6 (c) and (d)) were compared with

the reference to evaluate errors. The difference between the top and middle rows are shown in Figure 6.6 (e) and (f). As shown, the error happens mainly on the boundaries of compartments. The errors in Figure 6.6 (e) are dominantly in the signal-void area (i.e., the plastic separators between compartments). Therefore, they have little or no impact on the actual water-only image. The large errors on the bottom left of Figure 6.6 (f) may come from the low signal due to the coil sensitivity in the area. In both images, note that most error pixels on the boundary are due to low-resolution of the SEA reconstruction. These errors are expected to be reduced as the spatial resolution of SEA images is improved by on-going technical developments.

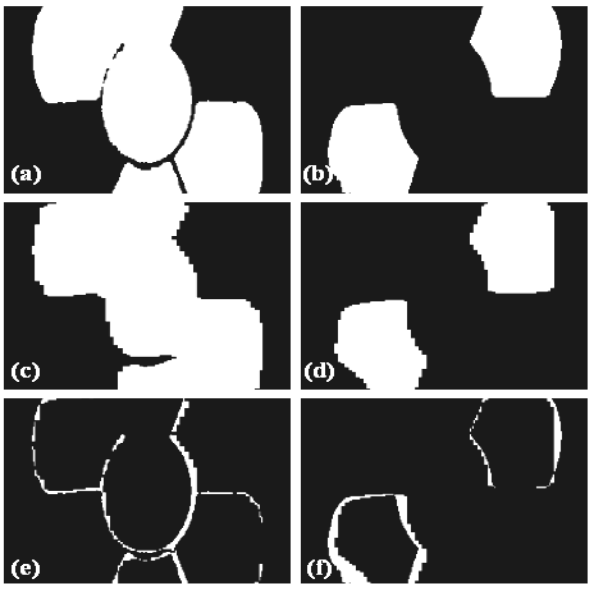

Fig 6.6 Evaluation of the water/fat separation accuracy. (a) water mask manually extracted from 256 × 256 high-resolution reference phantom image, (b) the corresponding fat mask, (c) and (d) water and fat masks from the proposed method, (e) and (f) error maps between (a) and (c), and (b) and (d), respectively. Note that the most errors are located on the trivial areas (plastic separators) or boundaries due to low resolution of the SEA image.

To evaluate robustness of the proposed line-by-line phase correction algorithm, zero-mean complex Gaussian random noise with different variance was added to the acquired signal. The water/fat maps produced from the corresponding SEA images are compared with reference water/fat maps shown in Figure 6.6 (c) and (d). Binary water/fat maps were exclusively (i.e. 0 is assigned to one map, and 1 is assigned to the other map) calculated by comparing signal intensity of two decomposed images for each pixel within ROI (i.e. combined water/fat maps in Figure 6.6 (c) and (d)). The Figure 6.7 shows the percent of the number of water/fat pixel changes within ROI is plotted as a function of the relative noise level to the baseline noise variance acquired from the original SEA image. The variance of the noise, σ, is computed from a 10 by 30 pixel region in the background area.

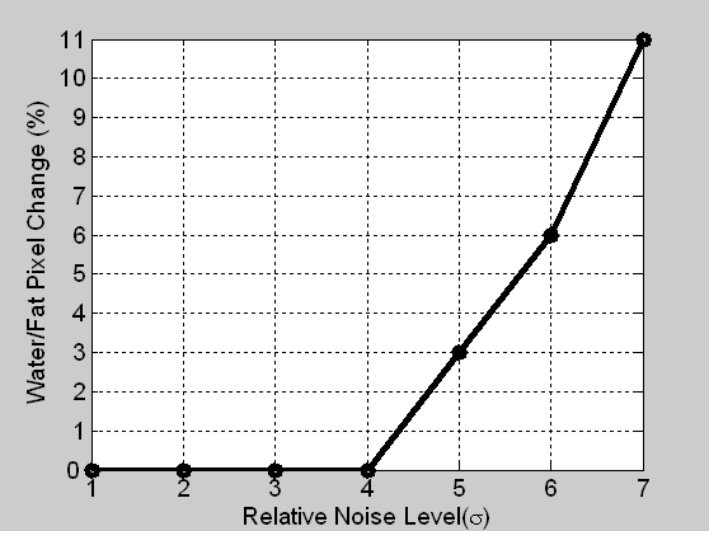

Fig 6.7 Variations of the water/fat pixel numbers (normalized by the total number of water and fat pixels in the references) as a function of additive zero-mean Gaussian noise. The graph shows that the algorithm is robust against additive noise in a large range.

Interestingly, in a large range of added noise levels (σ to 4σ), the identified water/fat pixels essentially have no change, indicating that the proposed 1-D region-growing algorithm is robust against the additive noise. Only when the relative noise level continued to rise (> 4σ), significant changes in water/fat decomposition occurred. The change rate is apparently linear. With 7σ of the relative noise level, the change rate is still below 11%.

VI.4 Discussion

In this chapter, we developed an ultra-fast and auto-calibrating contrast-enhanced SEA imaging technique, which can acquire 2-D water-only and fat-only images only using a single echo and without requiring any time-consuming calibration scan. Using the proposed technique, scan time was accelerated by 192 times compared with three-point Dixon techniques (4-6), which are requiring three sets of fully-encoded images for Dixon data acquisition and phase correction. Here, a factor of 64 is from SEA acceleration and a factor of 3 is from the single-echo Dixon technique using auto-calibrating phase correction ($192 = 64 \times 3$). In the phantom study, clearly decomposed 2-D water-only and fat-only slice images could be acquired with a single-echo using the proposed technique. This technique is expected to be useful to improve image-contrast by fat-suppression and to provide more accurate dynamic information.

There are several potential issues associated with the proposed phase correction algorithm. First, it requires that the non-chemical shift induced phase is spatially smooth within a channel. This condition is generally satisfied for typical spin-

echo SEA imaging, or well-shimmed gradient-echo SEA imaging. But caution should be used when dealing with areas with large susceptibility effects, because the phase variations can be very rapid. Second, there are possibly degenerate cases, such as two adjacent channels cover purely fat and purely water tissues respectively, which can make it difficult to use channel correlation to resolve water and fat ambiguity. However, this is a rare case for realistic biological tissues under normal experimental conditions. The other issue for the proposed phase correction algorithm is that tissues in FOV may not be connected. The signal void of the underlying channels may prevent successful use of channel correlation over the gap areas (56). In some cases, this issue may be alleviated by padding physical structures such as water bags between two isolated ROI regions.

CHAPTER VII

CONCLUSIONS AND FUTURE WORK

In this dissertation, new phase-sensitive MR techniques were developed to (1) separate spectrally overlapped chemical species but with different T_1 times, (2) improve image-contrast, and (3) increase scan-efficiency.

First, we developed a robust post-processing phase correction algorithm based on an adaptive Markov random field model. We demonstrated the proposed technique could reliably estimate the phase error map without requiring additional calibration scans. The primary benefit of using this technique is to improve scan-efficiency by completely eliminating time-consuming reference scans for phase correction. Another benefit is that we can prevent errors coming from patient motions between calibration and Dixon data acquisitions. The technique is expected to be useful to speed up water/fat imaging in potential applications such as obesity studies and screening.

Second, we developed a generalized chemical-shift imaging technique incorporating both T_1-contrast and chemical-shift. This technique can separate two signals having close resonance frequencies, as well as suppress multiple signals to improve image-contrast using only single image acquisition. A phantom experiment carried out on a 1.5 T clinical scanner demonstrated that the generalized chemical-shift imaging technique could achieve clear and uniform ternary signal decomposition for water (0 ppm), fat (3.5 ppm), and silicone signals (4.0 ppm), where resonance frequencies of fat and silicone signals are very close. The developed technique is

expected to extend the capability of Dixon imaging techniques in clinical applications such as contrast-enhanced breast tumor imaging for patients with silicone implants, where suppressing both strong silicone and fat signals is useful to capture lesion enhancement patterns, or suppressing both water and fat signals to find ruptures and leaking in the silicone implants.

Third, we developed a contrast-enhanced Dixon technique to extend the dynamic range of image intensity levels for Dixon techniques. A phantom study performed on a 4.7 T scanner demonstrated that clearly decomposed contrast-enhanced water and fat images could be obtained. The proposed technique improved the image-contrast by 1.6 times, as compared with a conventional single-point Dixon technique.

Finally, we developed a phase-sensitive MRI method integrated with a fully parallel ultra-fast SEA imaging technique. The technique takes advantage of the ultra-fast scan speed of the highly parallel imaging system and contrast-enhancing capability of Dixon image separation. A phantom study using a 64-channel SEA imaging system showed that decomposed 2-D water-only and fat-only images could be acquired with only a single echo, which can achieve a fast frame-rate of 1/TR frames per second, while providing improved image-contrast (by 2.4 times in this experiment) compared with the conventional SEA imaging technique.

Although penetration depth of the array is limited due to the small size of coil elements in one direction, the truly high frame-rate of SEA appeals to several potential applications in animal imaging. For example, the normal heartbeat rate of the mouse is 450 beats per minute, which is 7 ~ 8 times faster than that of the human. The normal

breathing frequency for the mouse is up to 200 times per minute (62). For future work, the developed technique can be applied to improve image-contrast for small lab animal studies, which are requiring fast image acquisition to overcome ghosting artifacts due to fast peristaltic movement of internal organs and breathing motion.

REFERENCES

1. Kellman P, Arai AE, McVeigh ER, Aletras AH. Phase-sensitive inversion recovery for detecting myocardial infarction using gadolinium delayed hyperenhancement. Magn Reson Med 2002;47:372-383.
2. Hou P, Hasan KM, Sitton CW, Wolinsky JS, Narayana PA. Phase-sensitive T1 inversion recovery imaging: a time-efficient interleaved technique for improved tissue contrast in neuroimaging. Am J Neuroradiol 2005;26:1432-1438.
3. Dixon W. Simple proton spectroscopic imaging. Radiology 1984;153:189-194.
4. Glover GH, Schneider E. Three-point Dixon technique for true water/fat decomposition with B0 inhomogeneity correction. Magn Reson Med 1991;18:371-383.
5. Glover GH. Multipoint Dixon technique for water and fat proton and susceptibility imaging. J Magn Reson Imaging 1991;1:521-530.
6. Wang Y, Li D, Haacke EM, Brown JJ. A three-point Dixon method for water and fat separation using 2D and 3D gradient-echo techniques. J Magn Reson Imaging 1998;8:703-710.
7. Tien RD. Fat-suppression MR imaging in neuroradiology. AJR Am J Roentgenol 1992;158:369-379.
8. Delfaut EM, Beltran J, Johnson G, Rousseau J, Marchandise X, Cotton A. Fat suppression in MR imaging: techniques and pitfalls. Radiological Society of North America 1999;19:373-382.

9. Kovanlikaya A, Mittelman SD, Ward A, Geffner ME, Dorey F, Gilsanz V. Obesity and fat quantification in lean tissues using three-point Dixon MR imaging. Pediatric Radiology 2005;35:601-607.
10. Haase A, Frahm J, Hanicke W, Matthaei D. 1H NMR chemical shift selective (CHESS) imaging. Phys Med Biol 1985;30(4):341-344.
11. Keller PJ, Hunter WW. Schmalbrock P. Multisection fat-water imaging with chemical shift selective presaturation. Radiology 1987;164(2):539-541.
12. Foster MA, Hutchison JM, Mallard JR, Fuller M. Nuclear magnetic resonance pulse sequence and discrimination of high- and low-fat tissues. Magn Reson Imaging 1984;2(3):187-192.
13. Bydder GM, Young IR. MR imaging: clinical use of the inversion recovery sequence. J Comput Assist Tomogr 1985;9(4):659-675.
14. Mai VM, Chen Q, Bankier AA, Zhang M, Hagspiel KD, Berr SS, Edelman RR. Imaging pulmonary blood flow and perfusion using phase-sensitive selective inversion recovery. Magn Reson Med 2000;43:793-795.
15. Christophe C, Muller MF, Baleriaux D, Kahn A, Pardou A, Perlmutter N, Szliwowski H, Segebarth C. Mapping of normal brain maturation in infants on phase-sensitive inversion-recovery MR imaging. Neuroradiology 1990;32:173-178.
16. Gorczyca DP, Sinha S, Ahn CY, DeBruhl ND. Hayes MK. Gausche VR. Shaw WW. Bassett LW. Silicone breast implants in vivo: MR imaging. Radiology 1992;185:407-410.
17. Ma J, Choi H, Stafford RJ, Miller MJ. Silicone-specific imaging using an

inversion-recovery-prepared fast three-point Dixon technique. J Magn Reson Imaging 2004;19:298-302.

18. Caskey CI, Berg WA, Anderson ND, Sheth S, Chang BW, Hamper UM. Breast implant rupture: diagnosis with US. Radiology 1994;190:819-823.
19. Kessler DA. The basis of the FDA's decision on breast implants. N Engl J Med 1992;326:1713-1715.
20. Blair P. A staff report by the human resources and intergovernmental relations subcommittee of the committee on governmental relations. In: The FDA's regulation of silicone breast implants. Washington, DC: U.S. Government Printing Office; 1999. p 24.
21. deCamera DL, Sheridan JM, Kammer BA. Rupture and aging of silicone gel breast implants. In: Plastic Surgery Forum: 60th Annual Scientific Meeting, Seattle, WA, 1991:244.
22. Cole-Beuglet C, Schwartz C, Kurtz AB, Patchefsky AS, Goldberg BB. Ultrasound mammography for the augmented breast. Radiology 1983;146:737-742.
23. Herzog P. Silicone granutomas: detection by ultrasonography. Plast Reconstr Surg 1989;84:856-857.
24. Harris KM, Cannot MA, Shestak KC, Losken HW, Tobon H. Silicone implant rupture: detection with US. Radiology 1993;187:761-768.
25. Roscubet KA, Ikeda DM, Forrest ME, Oneal RM, Rubin JM, Jeffries DO, Helvie MA. Ruptured gel-filled silicone breast implants: sonographic findings in 19 cases. AJR Am J Roentgenol 1992;159:711-716.

26. Levine RA, Collins TL. Definitive diagnosis of breast implant rupture by uttrasonography. Plast Reconstr Surg 1991;87:1126-1128.

27. Wolff SD, Balaban RS. Magnetization transfer contrast (MTC) and tissue water proton relaxation in vivo. Magn Reson Med 1989;10:135-144.

28. Po J, Margolis D, Cunningham C, Herfkens R, Ikeda D, Daniel B. Water-selective spectral-spatial contrast-enhanced breast MRI for cancer detection in patients with extracapsular and injected free silicone. Magn Reson Imaging 2006;24(10):1363-1367.

29. Ma J, Son JB, Bankson JA, Stafford RJ, Choi H, Ragan D. A fast spin echo two-point Dixon technique and its combination with sensitivity encoding for efficient T2-weighted imaging. Magn Reson Imaging 1998;8:703-710.

30. Simon JH, Szumowski J. Chemical shift imaging with paramagnetic contrast material enhancement for improved lesion depiction. Radiology 1989;171:539-543.

31. Reeder SB, Markl M, Yu H, Hellinger JC, Herfkens RJ, Pelc NJ. Cardiac CINE imaging with IDEAL water-fat separation and steady-state free precession. J Magn Reson Imaging 2005;22:44-52.

32. Reeder SB, Pineda AR, Yu H. Water-fat separation with IDEAL-SPGR. In: Proceedings of the 14th Annual Scientific Meeting of ISMRM, Seattle, WA, 2006:105.

33. Reeder SB, Wen Z, Yu H. Multicoil Dixon chemical species separation with an iterative least-squares estimation method. Magn Reson Med 2004;51:35-45.

34. Lauterbur PC. Image formation by induced local interactions: examples employing

nuclear magnetic resonance. Nature 1973;242:190-191.

35. Enderle JD, Blanchard SM, Bronzino JD. Introduction to biomedical engineering. San Diego: Academic Press; 2000. p 1062.
36. Haacke EM, Brown RW, Thompson MR, Venkatesan R. Magnetic resonance imaging: physical principles and sequence design. New York: J. Wiley & Sons; 1999. p 914.
37. Cho ZH, Jones JP, Singh M. Foundations of medical imaging. New York: Wiley & Sons; 1993. p 586.
38. Liang ZP, Lauterbur PC. Principles of magnetic resonance imaging: a signal processing perspective. New York: Wiley-IEEE Press; 1999. p 416.
39. Wright SM, McDougall MP, Brown DG. Single echo acquisition (SEA) MR imaging. In: Proceedings of the 11th Annual Meeting of ISMRM, Toronto, ON, CA, 2003:23.
40. McDougall MP, Wright SM, Brown DG. A 64 channel planar RF coil array for parallel imaging at 4.7 Tesla. In: Proceedings of the 11th Annual Meeting of ISMRM, Toronto, ON, CA, 2003:472.
41. McDougal MP, Wright SM. Phase compensation in single echo acquisition imaging. IEEE Eng Med Biol Mag 2005;24(6):17-22.
42. Wright SM, McDougall MP, Yallapragada N. Ultra-Fast MR velocity measurement using spin-tagging and single-echo acquisition (SEA) imaging. In: Proceedings of the 14th Annual Meeting of ISMRM, Seattle, WA, 2006:203.
43. Patrick JL, Haacke EM, Hahn JE. Water/fat separation and chemical-shift artifact

correction using a single scan. In: Proceedings of the 4th Annual Scientific Meeting of ISMRM, New York, 1985:174.

44. Ma J. Breath-hold water and fat imaging using a dual-echo two-point Dixon technique with an efficient and robust phase-correction algorithm. Magn Reson Med 2004;52:415-419.

45. Son JB, Ji JX, Ma J. Three-dimensional T_1-weighted MR imaging using a one-point Dixon technique with arbitrary echo time. In: Proceedings of the 13th Annual Meeting of ISMRM, Miami, FL, 2005:893.

46. Bakker CJG, De Graff CN, Van Dijk P. Restoration of signal polarity in a set of inversion recovery NMR images. IEEE Trans Med Imaging 1984;18:371-383.

47. Gowland PA, Leach MO. A simple method for the restoration of signal polarity in multi-image inversion recovery sequences for measuring T1. Magn Reson Med 1991;18:224-231.

48. Markov AA. Extension of the limit theorems of probability theory to a sum of variables connected in a chain. New York: J. Wiley & Sons; 1999. p 914.

49. Geman S, Geman D. Stochastic relaxation, Gibbs distributions, and the Bayesian restoration of images. Machine Intell. 1984;6(6):721-741.

50. Chen CW, Zebker HA. Two-dimensional phase unwrapping with use of statistical models for cost functions in nonlinear optimization. J. Opt. Soc. Amer. A 2001;18(2):338-351.

51. Leitao JMN, Figueiredo MAT. Absolute phase image reconstruction: a stochastic nonlinear filtering approach. IEEE Trans Image Process. 1998;7(6):868-882.

52. Koetter R, Frey BJ, Petrovic N, Munson DC. Unwrapping phase images by propagating probabilities across graphs. In: Proceedings of IEEE Int Conf Acoustics, Speech, and Signal Processing 2001:1845-1848.

53. Ying L, Liang ZP, Munson DC, Koetter R, Frey BJ. Unwrapping of MR phase images using a Markov random field model. IEEE Trans Med Imaging 2006;25(1):128-136.

54. Li SZ. Markov random modeling in computer vision. London: Springer-Verlag; 1995. p 185-230.

55. Son JB, Ji JX. Auto-calibrated dynamic parallel MRI with phase-sensitive data. In: Proceedings of the 28th Annual International Conference of the IEEE EMBS 2006;751-754.

56. Xiang QS, An L. Water-fat imaging with direct phase encoding. J Magn Reson Imaging 1997;7(6):1002-1015.

57. McDougall MP. Single echo acquisition magnetic resonance imaging. PhD Dissertation, Texas A&M University 2004.

58. Sodickson D, Manning W. Simultaneous acquisition of spatial harmonics (SMASH): fast imaging with radiofrequency coil arrays. Magn Reson Med 1997;38:591-603.

59. Pruesmann K, Weiger M, Scheidegger M, Boesiger P. SENSE: Sensitivity encoding for fast MRI. Magn Reson Med 1999;42:952-962.

60. Griswold M, Jakob P, Nittka M, Goldfarb J, Haase A. Partially parallel imaging with localized sensitivities (PILS). Magn Reson Med 2000;47:602-609.

61. Griswold M, Jakob P, Heidemann R, Nittka M, Jellus V, Wang J, Kiefer B, Haase A. Generalized auto-calibrating partially parallel acquisitions (GRAPPA). Magn Reson Med 2002;47:1202-1210.

62. Kleinman LI, Radford EP. Ventilation standard for small mammals. J Appl Physiol 1964;19:360-362.

VITA

Name: Jong Bum Son

Address: 463-926 South Korea Gyeonggi-Do Sungnam-Si Bundang-Gu Yatap-Dong Tap-Mael Daewoo APT 201Dong 1002Ho

Email Address: dante.son@gmail.com

Education: B.S., Electrical Engineering, Korea University, 1997

Intern, Imaging Physics, The University of Texas M. D. Anderson Cancer Center, 2005

Ph.D., Electrical Engineering, Texas A&M University, 2007